

REPORT DOCUMENTATION PAGE			Form Approved OMB NO. 0704-0188		
<p>The public reporting burden for this collection of information is estimated to average 1 hour per response, including the time for reviewing instructions, searching existing data sources, gathering and maintaining the data needed, and completing and reviewing the collection of information. Send comments regarding this burden estimate or any other aspect of this collection of information, including suggestions for reducing this burden, to Washington Headquarters Services, Directorate for Information Operations and Reports, 1215 Jefferson Davis Highway, Suite 1204, Arlington VA, 22202-4302. Respondents should be aware that notwithstanding any other provision of law, no person shall be subject to any penalty for failing to comply with a collection of information if it does not display a currently valid OMB control number.</p> <p>PLEASE DO NOT RETURN YOUR FORM TO THE ABOVE ADDRESS.</p>					
1. REPORT DATE (DD-MM-YYYY) 12-10-2013		2. REPORT TYPE Final Report		3. DATES COVERED (From - To) 12-Aug-2009 - 12-Jul-2013	
4. TITLE AND SUBTITLE Metrology with Weak Value Amplification and Related Topics: Final Report - Army Research Office, Grant No. W911NF-09-0-01417			5a. CONTRACT NUMBER W911NF-09-1-0417		
			5b. GRANT NUMBER		
			5c. PROGRAM ELEMENT NUMBER 611102		
6. AUTHORS Andrew N. Jordan, John C. Howell			5d. PROJECT NUMBER		
			5e. TASK NUMBER		
			5f. WORK UNIT NUMBER		
7. PERFORMING ORGANIZATION NAMES AND ADDRESSES University of Rochester ORPA 512 Hylan Building Rochester, NY 14611 -3847			8. PERFORMING ORGANIZATION REPORT NUMBER		
9. SPONSORING/MONITORING AGENCY NAME(S) AND ADDRESS(ES) U.S. Army Research Office P.O. Box 12211 Research Triangle Park, NC 27709-2211			10. SPONSOR/MONITOR'S ACRONYM(S) ARO		
			11. SPONSOR/MONITOR'S REPORT NUMBER(S) 56353-PH-QC.15		
12. DISTRIBUTION AVAILABILITY STATEMENT Approved for Public Release; Distribution Unlimited					
13. SUPPLEMENTARY NOTES The views, opinions and/or findings contained in this report are those of the author(s) and should not be construed as an official Department of the Army position, policy or decision, unless so designated by other documentation.					
14. ABSTRACT This report summarizes our accomplishments in the past 3+1 years concerning our investigation into the advantages of weak value approaches to precision measurements, as well as other investigations into weak measurements and weak values. The report is divided into two sections: The first focuses on a detailed discussion of results concerning applications and advantages of weak value amplification techniques to precision measurement. Here, we discuss four separate but connected projects. The first concerns the possibility of reusing the rejected photons					
15. SUBJECT TERMS Precision measurement, weak value amplification, weak and generalized measurements					
16. SECURITY CLASSIFICATION OF:			17. LIMITATION OF ABSTRACT UU	15. NUMBER OF PAGES	19a. NAME OF RESPONSIBLE PERSON Andrew Jordan
a. REPORT UU	b. ABSTRACT UU	c. THIS PAGE UU			19b. TELEPHONE NUMBER 585-275-2418

Report Title

Metrology with Weak Value Amplification and Related Topics: Final Report - Army Research Office, Grant No. W911NF-09-0-01417

ABSTRACT

This report summarizes our accomplishments in the past 3+1 years concerning our investigation into the advantages of weak value approaches to precision measurements, as well as other investigations into weak measurements and weak values. The report is divided into two sections: The first focuses on a detailed discussion of results concerning applications and advantages of weak value amplification techniques to precision measurement. Here, we discuss four separate but connected projects. The first concerns the possibility of reusing the rejected photons in the postselection portion of the weak value amplification. We examine a sequence of polarized laser pulses effectively trapped inside an interferometer using a Pockels cell and polarization optics. In principle, all photons can be post-selected, which will improve the measurement sensitivity. The main advantage of such a recycling scheme is an effective power increase, while maintaining an amplified deflection. The second project concerns the technical merits of weak value amplification. We consider models of several different types of technical noise in an optical context and show that weak value amplification techniques (which only use a small fraction of the photons) compare favorably with standard techniques (which uses all of them). Using the Fisher information metric, we demonstrate that weak value techniques give much higher information over conventional methods in some cases, showing a fundamental advantage. We identify other cases where the standard technique has higher Fisher information, but the statistical estimator needed to uncover that information is technically difficult to implement, demonstrating technical advantages. We also discuss a third project using our interferometric weak value technique to make precision frequency measurements on an optical beam, reporting a resolution of 129 ± 7 kHz per root Hz with only 2 mW of continuous-wave power. The fourth project deals with a weak value inspired phase amplification technique. We monitor the relative phase between two paths of a slightly misaligned interferometer by measuring the average position of a split-Gaussian mode in the dark port. Although we monitor only the dark port, we show that the signal varies linearly with phase and that we can obtain similar sensitivity to balanced homodyne detection. We relate the effect to an inverse weak value.

The second main part of the report concerns results related to weak measurements and weak values, but not directly related to the amplification issue. We give a brief survey of our results in this area. We have investigated weak measurements as a test of quantum mechanics, by deriving generalized Leggett-Garg inequalities for multiple parties and violating them with entangled photons. We have made a systematic analysis of coupled electronic Mach-Zehnder interferometers, where one is used as a detector for the other; this set-up can also be used for parameter estimation. We have extensively investigated a new approach to generalized measurement we call contextual values, which gives a precise connection between an indirectly measured system and the outcomes of the detector by assigning a set of generalized eigenvalues to each detector outcome. This assignment permits a principled definition of a conditioned average, which limits to the weak value under certain conditions that are usually satisfied in the laboratory. We have also discussed the significance of the imaginary part of the weak value. While the imaginary weak value is very useful in amplification (parameter estimation) experiments, we show it has no direct connection any conditioned average of the operator itself. Often the weak value is restricted to the weak limit, where the measurement interaction is infinitesimally small. We have shown that the general structure of the weak value is actually universal for any interaction strength and any meter wavefunction, so long as the form of the interaction is of the von Neumann type. We have also investigated the concept of the quantum instrument, and how it directly deals with observable events in the lab, without using states or observables.

Enter List of papers submitted or published that acknowledge ARO support from the start of the project to the date of this printing. List the papers, including journal references, in the following categories:

(a) Papers published in peer-reviewed journals (N/A for none)

<u>Received</u>	<u>Paper</u>
-----------------	--------------

08/18/2011	2.00	John Howell, David Starling, P. Dixon, Andrew Jordan. Precision frequency measurements with interferometric weak values, Physical Review A, (12 2010): 0. doi: 10.1103/PhysRevA.82.063822
10/12/2013	4.00	P. Ben Dixon, Nathan S. Williams, David J. Starling, Andrew N. Jordan, John C. Howell. Continuous phase amplification with a Sagnac interferometer, Physical Review A, (07 2010): 0. doi: 10.1103/PhysRevA.82.011802
10/12/2013	5.00	J. Dressel, S. Agarwal, A. N. Jordan. Contextual Values of Observables in Quantum Measurements, Physical Review Letters, (06 2010): 0. doi: 10.1103/PhysRevLett.104.240401
10/12/2013	7.00	J. Dressel, A. N. Jordan. Contextual-value approach to the generalized measurement of observables, Physical Review A, (02 2012): 0. doi: 10.1103/PhysRevA.85.022123
10/12/2013	8.00	J. Dressel, A. N. Jordan. Significance of the imaginary part of the weak value, Physical Review A, (01 2012): 0. doi: 10.1103/PhysRevA.85.012107
10/12/2013	9.00	Justin Dressel, Andrew N. Jordan. Weak Values are Universal in Von Neumann Measurements, Physical Review Letters, (12 2012): 0. doi: 10.1103/PhysRevLett.109.230402
10/12/2013	10.00	Justin Dressel, Andrew N. Jordan. Quantum instruments as a foundation for both states and observables, Physical Review A, (08 2013): 0. doi: 10.1103/PhysRevA.88.022107
10/12/2013	11.00	Justin Dressel, Kevin Lyons, Andrew N. Jordan, Trent M. Graham, Paul G. Kwiat. Strengthening weak-value amplification with recycled photons, Physical Review A, (08 2013): 0. doi: 10.1103/PhysRevA.88.023821
10/12/2013	12.00	Y. Choi, A. N. Jordan, J. Dressel. Measuring which-path information with coupled electronic Mach-Zehnder interferometers, Physical Review B, (01 2012): 0. doi: 10.1103/PhysRevB.85.045320
TOTAL:	9	

Number of Papers published in peer-reviewed journals:

(b) Papers published in non-peer-reviewed journals (N/A for none)

<u>Received</u>	<u>Paper</u>
-----------------	--------------

08/18/2011	1.00	J. Dressel, C. Broadbent, J. Howell, A. Jordan. Experimental Violation of Two-Party Leggett-Garg Inequalities with Semiweak Measurements, Physical Review Letters, (1 2011): 0. doi: 10.1103/PhysRevLett.106.040402
TOTAL:	1	

Number of Papers published in non peer-reviewed journals:

(c) Presentations	
Weak values: the progression from quantum foundations to tool, University of Geneva, physics seminar, August 2012	
Increase of Signal-to-Noise Ratio in Weak Value Measurements, C. Byard, T. Graham, A. Danan, L. Vaidman, A. N. Jordan, P. Kwiat, Yakir Aharonov Festschrift, Chapman University, 2012	
Weak Values: The Progression from Quantum Foundations to Tool, Andrew N. Jordan, Jeff Tollaksen, Yakir Aharonov Festschrift, Chapman University, 2012	
Weak values - the progression from quantum foundations to tool, Cancun, Mexico, Nov. 2012, LAOP workshop.	
Contextual values as a foundation for a unique Weak Value, Justin Dressel and Andrew N. Jordan, quantum retrocausation: theory and experiment, June 2011, San Diego, California	
Precision measurement with weak values - Cross Border workshop, Rochester, NY, 2011.	
Weak value amplification, FQMT'11: Frontiers of Quantum and Mesoscopic Thermodynamics (Prague, Czech Republic, 25–30 July 2011)	
Number of Presentations:	7.00

Non Peer-Reviewed Conference Proceeding publications (other than abstracts):	
Received	Paper
TOTAL:	
Number of Non Peer-Reviewed Conference Proceeding publications (other than abstracts):	

Peer-Reviewed Conference Proceeding publications (other than abstracts):	
Received	Paper
TOTAL:	
Number of Peer-Reviewed Conference Proceeding publications (other than abstracts):	

(d) Manuscripts

Received Paper

08/18/2011 3.00 J. Dressel, Y. Choi, A. N. Jordan. Measuring Which-Path Information with Coupled Electronic Mach-Zehnder Interferometers ,
arXiv:1105.2587 (05 2011)

10/12/2013 13.00 Julián Martínez-Rincón, John C. Howell, Andrew N. Jordan. Technical advantages for weak value amplification: When less is more,
ArXiv: 1309.5011 (09 2013)

10/12/2013 14.00 Justin Dressel , Mehul Malik , Filippo M. Miatto , Andrew N. Jordan , Robert W. Boyd. Understanding Quantum Weak Values: Basics and Applications,
ArXiv: 1305.7154 (05 2013)

TOTAL: 3

Number of Manuscripts:

Books

Received Paper

TOTAL:

Patents Submitted

Patents Awarded

Awards

Graduate Students

<u>NAME</u>	<u>PERCENT SUPPORTED</u>	Discipline
Yunjin Choi	0.10	
Justin Dressel	1.00	
David Starling	1.00	
FTE Equivalent:	2.10	
Total Number:	3	

Names of Post Doctorates

<u>NAME</u>	<u>PERCENT SUPPORTED</u>
-------------	--------------------------

FTE Equivalent:

Total Number:

Names of Faculty Supported

<u>NAME</u>	<u>PERCENT SUPPORTED</u>	National Academy Member
Andrew N. Jordan	0.50	
John Howell	0.20	
FTE Equivalent:	0.70	
Total Number:	2	

Names of Under Graduate students supported

<u>NAME</u>	<u>PERCENT SUPPORTED</u>
-------------	--------------------------

FTE Equivalent:

Total Number:

Student Metrics

This section only applies to graduating undergraduates supported by this agreement in this reporting period

The number of undergraduates funded by this agreement who graduated during this period:	0.00
The number of undergraduates funded by this agreement who graduated during this period with a degree in science, mathematics, engineering, or technology fields:.....	0.00
The number of undergraduates funded by your agreement who graduated during this period and will continue to pursue a graduate or Ph.D. degree in science, mathematics, engineering, or technology fields:.....	0.00
Number of graduating undergraduates who achieved a 3.5 GPA to 4.0 (4.0 max scale):.....	0.00
Number of graduating undergraduates funded by a DoD funded Center of Excellence grant for Education, Research and Engineering:	0.00
The number of undergraduates funded by your agreement who graduated during this period and intend to work for the Department of Defense	0.00
The number of undergraduates funded by your agreement who graduated during this period and will receive scholarships or fellowships for further studies in science, mathematics, engineering or technology fields:	0.00

Names of Personnel receiving masters degrees

<u>NAME</u>

Total Number:

Names of personnel receiving PHDs

<u>NAME</u>
Justin Dressel (1)
David Starling (1)

Total Number: 2

Names of other research staff

<u>NAME</u>	<u>PERCENT_SUPPORTED</u>
FTE Equivalent:	
Total Number:	

Sub Contractors (DD882)

Inventions (DD882)

Scientific Progress

See Attachment

Technology Transfer

Metrology with Weak Value Amplification and Related Topics: Final Report - Army Research Office, Grant No. W911NF-09-0-01417

Andrew N. Jordan and John C. Howell

Department of Physics and Astronomy, University of Rochester, Rochester, New York 14627, USA

(Dated: October 12, 2013)

This report summarizes our accomplishments in the past 3+1 years concerning our investigation into the advantages of weak value approaches to precision measurements, as well as other investigations into weak measurements and weak values. The report is divided into two sections: The first focuses on a detailed discussion of results concerning applications and advantages of weak value amplification techniques to precision measurement. Here, we discuss four separate but connected projects. The first concerns the possibility of reusing the rejected photons in the postselection portion of the weak value amplification. We examine a sequence of polarized laser pulses effectively trapped inside an interferometer using a Pockels cell and polarization optics. In principle, all photons can be post-selected, which will improve the measurement sensitivity. The main advantage of such a recycling scheme is an effective power increase, while maintaining an amplified deflection. The second project concerns the technical merits of weak value amplification. We consider models of several different types of technical noise in an optical context and show that weak value amplification techniques (which only use a small fraction of the photons) compare favorably with standard techniques (which uses all of them). Using the Fisher information metric, we demonstrate that weak value techniques give much higher information over conventional methods in some cases, showing a fundamental advantage. We identify other cases where the standard technique has higher Fisher information, but the statistical estimator needed to uncover that information is technically difficult to implement, demonstrating technical advantages. We also discuss a third project using our interferometric weak value technique to make precision frequency measurements on an optical beam, reporting a resolution of 129 ± 7 kHz per root Hz with only 2 mW of continuous-wave power. The fourth project deals with a weak value inspired phase amplification technique. We monitor the relative phase between two paths of a slightly misaligned interferometer by measuring the average position of a split-Gaussian mode in the dark port. Although we monitor only the dark port, we show that the signal varies linearly with phase and that we can obtain similar sensitivity to balanced homodyne detection. We relate the effect to an inverse weak value.

The second main part of the report concerns results related to weak measurements and weak values, but not directly related to the amplification issue. We give a brief survey of our results in this area. We have investigated weak measurements as a test of quantum mechanics, by deriving generalized Leggett-Garg inequalities for multiple parties and violating them with entangled photons. We have made a systematic analysis of coupled electronic Mach-Zehnder interferometers, where one is used as a detector for the other; this set-up can also be used for parameter estimation. We have extensively investigated a new approach to generalized measurement we call contextual values, which gives a precise connection between an indirectly measured system and the outcomes of the detector by assigning a set of generalized eigenvalues to each detector outcome. This assignment permits a principled definition of a conditioned average, which limits to the weak value under certain conditions that are usually satisfied in the laboratory. We have also discussed the significance of the imaginary part of the weak value. While the imaginary weak value is very useful in amplification (parameter estimation) experiments, we show it has no direct connection any conditioned average of the operator itself. Often the weak value is restricted to the weak limit, where the measurement interaction is infinitesimally small. We have shown that the general structure of the weak value is actually universal for any interaction strength and any meter wavefunction, so long as the form of the interaction is of the von Neumann type. We have also investigated the concept of the quantum instrument, and how it directly deals with observable events in the lab, without using states or observables.

This report concerns published scientific findings made by the Jordan and Howell group for the research funded by the Army Research Office for the year 2010-2013 (including one year of no-cost extension). The main theme of the proposal is the use of weak values and weak measurements for the purposes of precision measurement, in particular parameter estimation. A subsidiary theme is investigation into fundamental aspects of weak measurements and weak values, in order to better understand their meaning and applications. On the first theme, we summarize our findings of four projects supported by this grant: The use of photon recycling ideas to further enhance the sensitivity of this technique, a detailed analysis of various technical advantages of weak value amplification techniques, a practical demonstration of precise frequency measurements, and a second experiment making precise phase measurements. We go to briefly summarize our supporting theoretical and experimental results. These include utilizing the weak value as a test of quantum mechanics, results on weak measurements and values in condensed matter systems, including a recently experimentally realized coupled electronic Mach-Zehnder interferometers (MZI), the theoretical development of the meaning of the imaginary weak values used in the amplification papers, and the universal form of a conditioned average once away from the weak interaction limit.

A long standing goal in optics is the development and improvement of precision optical metrology. In the first paper on weak values in 1988 [1], Aharonov, Albert and Vaidman suggested that the weak value effect might be used as an amplifier in order to measure (in the case they were considering) the value of a small magnetic field by looking at the anomalously large deflection of a beam of atoms traversing a Stern-Gerlach apparatus. The general validity of this weak value effect was later shown experimentally in an optical context by Ritchie *et al.* [2], who replaced the magnetic spin with transverse polarization, and Brunner *et al.* [3], who illustrated the pervasiveness of the weak value effect in common optical telecom networks.

More recently, the amplification properties of this weak value effect have been exploited in similar optical systems to precisely measure beam deflection [4–10], frequency shifts [11], phase shifts [12, 13], time delays [14], velocity measurements [15], and even temperature shifts [16], by using either polarization or which-path degrees of freedom. In most of these experiments, the weak value amplification (WVA) technique met and even surpassed the sensitivity of standard techniques in the field. For a recent review of this and related weak value research, see Ref. [17]. Although many aspects of these optical experiments can be described using classical wave optics [18], the analysis using quantum techniques provides additional insight and allows for future extension to cases with no classical counterpart. Hence, we shall continue to use a quantum approach in this work as well.

Table of Contents

Part I: Weak value amplification: recycling, technical advantages, and frequency measurements
Sec. I, Increasing precision of weak value amplification techniques with recycled photons
Sec. II, Analysis of advantages of weak value amplification in the presence of technical noise
Sec. III, Weak Value enhanced precision frequency measurements
Sec. IV, Precision phase difference measurements

Part II: Summary of further results concerning weak values and weak measurements
A. Contextual Values
B. Two-Party Leggett-Garg Inequalities with Semiweak Measurements
C. Measuring Which-Path Information with Coupled Electronic Mach-Zehnder Interferometers
D. The significance of the imaginary part of the weak value
E. Weak values are universal in von Neumann measurements
F. Quantum instruments as a foundation for both states and observables

List of Figures

Fig. 1, Cyclic weak measurement geometry.
Fig. 2, Detector profile for strongly misaligned regime.
Fig. 3, Detector profile for weak-value regime.
Fig. 4, Detector profile for inverse Weak-value regime.
Fig. 5, Normalized split-detection response for a collimated pulse.
Fig. 6, Response for a collimated pulse stabilized by parity flipping.
Fig. 7, SNR gain versus traversal number for a collimated pulse.
Fig. 8, The effect of propagation and different diverging lens choices on the SNR.
Fig. 9, Representation on the Bloch sphere of the preselection and postselection states.
Fig. 10, Plots of numerators of weak value expression.
Fig. 11, Geometries for two strategies to detect momentum kick k given angular jitter of momentum q .
Fig. 12, Frequency measurement geometry.
Fig. 13, Position of the postselected beam profile versus input laser frequency.

Fig. 14, Noise spectrum of the experiment.

Fig. 15, Experimental setup for phase measurements.

Fig. 16, Post-selected split-Gaussian mode for phase measurement.

Fig. 17, Transverse momentum shift imparted by the piezo-actuated mirror.

Fig. 18, Experimental comparison of split-detection to balanced homodyne.

Part I

Weak value amplification: recycling, technical advantages, and frequency measurements

I. INCREASING PRECISION OF WEAK VALUE AMPLIFICATION TECHNIQUES WITH RECYCLED PHOTONS

The first work in this report [19] concerns a theoretical recycling proposal with recycled photons, in order to also make use of the photons lost through the bright port in the weak value scheme. Consider our earlier experiment [5], where the tilt of a moving mirror within an interferometer is detected from the signal on a split-detector. While this setup has a sub-picoradian resolution with only milliwatts of laser power, there are a number of ways this can be improved to yield even greater sensitivity.

A generic shortcoming of weak-value-related metrological techniques is the fact that only a small fraction of the events are “post-selected”, while the vast majority of events are intentionally thrown away. The main goal of the current work is to investigate how this situation can be further improved if those events are recycled. This will be done by taking photons which are not post-selected and reinjecting them back into the interferometer, so that eventually, every photon can be post-selected in principle. We will see that this strategy does indeed lead to an improvement in the signal-to-noise ratio (SNR) of the desired parameter, effectively given by the power increase of the split-detection signal. Moreover, since the existing single-pass weak-value amplification already achieves the sensitivity of standard measurement techniques (such as homodyne detection) but with lower technical noise [9], the improvements from recycling should *exceed* the sensitivity of the standard techniques. We note that because we employ not just a single pass, but many passes of a given photon through the interferometer, the simple weak value formula used in the first paper on the subject [5] will no longer suffice, and we must develop a theoretical formalism for multiple passes that will account for the amplification of the deflection, as well as the probability of reaching the detector after some number of traversals.

While the recycling scheme is an important advance in its own right (and can be generically applied to all weak value amplification schemes), it also lends itself to further enhancement if combined with other precision metrology techniques currently in use. For example, the inclusion of a spatial filter or parity-flipping element to Zeno-stabilize the beam, or the use of a squeezed reference beam [20–23] could significantly reduce degradation effects and quantum noise, respectively. The recycling technique, therefore, sets the stage for combined weak value/quantum light amplification strategies for future research. Furthermore, though our present work focuses on a novel pulsed recycling method, possible extensions to continuous wave operation may allow for the use of power recycling [24] and signal recycling [25] techniques, both of which are in use in modern gravitational wave detectors [26, 27].

A. Qualitative Arguments

Our baseline for comparison will be the Rochester continuous wave (CW) Sagnac interferometric scheme described in [5, 9, 18]. We wish to improve the detected SNR by using a combination of pulsed laser operation with the same average power output and a design that sends the undetected portion of each pulse back into the interferometer. Such a setup is illustrated in Figure 1 for reference. However, before committing to a particular recycling design we can make fairly general estimations about the increases in sensitivity that we expect from any similar recycling scheme.

1. Characteristic Time Scales

The constraints on how much we can increase the power collected by the dark port detector in order to improve the measurement sensitivity depend crucially on the relative time scales involved, which include:

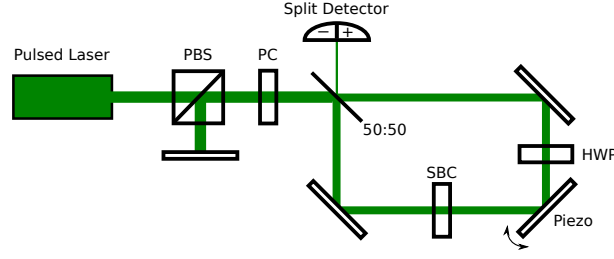


FIG. 1. Simple cyclic weak measurement scheme. A laser emits a pulse of horizontal (H) polarization through a polarizing beam splitter (PBS), which travels through an active Pockels cell (PC) that rotates the polarization to vertical (V), after which it enters a Sagnac interferometer through a 50:50 beam splitter. Inside the interferometer the combination of half-wave plate (HWP) and Soleil-Babinet compensator (SBC) rotates the pulse polarization back to H with a relative tunable phase shift of ϕ between the clockwise (\odot) and counter-clockwise (\ominus) traveling paths. The piezo-driven mirror imparts a transverse momentum kick k that differs by a sign for the \odot and \ominus paths. A split detector is placed at the dark port to measure a resulting pulse deflection. The H-polarized part of the pulse that exits the bright port is rotated again by the active PC back to V before being confined by the PBS and mirror to return the pulse to the interferometer through the PC, now *inactive*.

Symbol	Description	Estimate
τ	Laser pulse duration	5 fs - 1 ns
T	Laser repetition period	1 ns - 1 s
T_r	Traversal period	1 ns - 10 ns
T_g	Gating time	2 ns
T_p	Minimum inter-pulse spacing	$\tau + T_g$

TABLE I. Relevant time scales for a recycling experiment.

1. The pulse duration τ being emitted by the laser. For typical lasers this can vary between 1 ns and 5 fs reasonably, which correspond to pulse lengths of 0.3 m and 1.5 μm , respectively.
2. The repetition period $T = 1/f$ of the laser. For typical lasers the repetition rate f can vary from 1 Hz to several GHz reasonably.
3. The traversal period T_r of the interferometer setup. This is determined by the physical size of the setup. As an upper-bound estimate, a 3 m long recycling setup will have a total period of 10 ns.
4. The gating time T_g for adding new pulses to the interferometer. This will determine the minimum inter-pulse spacing $T_p = \tau + T_g$ inside the interferometer. This also must be strictly less than the time between pulses emitted by the laser $T_g < T - \tau$ so that every new laser pulse can be injected. For a Pockels cell, $T_g \approx 2$ ns.

These are summarized in Table I.

We assume in what follows that $\tau < T_p < T_r$, so that at least one pulse can be trapped inside the interferometer. We also assume that the average power output P of the pulsed laser is equal to the average power of a comparison CW beam. As a result, the average power of each individual pulse will be increased by a factor T/τ from the reference CW beam.

2. Detector SNR

The SNR is a useful indicator for the sensitivity of the measurement, since a signal producing an SNR of unity indicates the smallest practically resolvable signal [21]. The detected SNR is defined as the ratio of the collected signal to the square root of the variance of that collected signal. Our raw signal $\langle S \rangle$ is a split-detection of the transverse profile of the beam, which measures the difference in photon number collected by each side of the detector, thereby providing information about the horizontal displacement of the beam. For small displacements, the variance of the split-detected signal is well approximated by the second moment, which is in turn proportional to the total photon number for position-uncorrelated photons (see, for example, Ref [21]).

The total accumulated split-detected signal scales linearly with the average collected energy, which can be factored into the average power at the detector P_d multiplying the collection duration t . The variance will be similarly

proportional to $P_d t$, so the SNR will scale as $P_d t / \sqrt{P_d t} = \sqrt{P_d t}$. Hence, the SNR can be increased either by waiting for a longer duration t or by increasing the average power P_d at the dark port detector. Our recycling scheme proposes to increase the average power collected within a fixed duration to increase the sensitivity.

In the original interferometric weak value scheme, the detector collected a power of $P_d = \eta P$, where η was the post-selected fraction of the total laser power P coming from the dark port. If we recycle the unused light, however, the average power P_d collected at the detector after r_T recycling passes in a laser repetition period T will have the modified form,

$$P_d = \sum_{n=1}^{r_T} (1 - \eta)^{n-1} \eta P = (1 - (1 - \eta)^{r_T}) P, \quad (1)$$

where η is the fraction of the input power that exits the dark port of the interferometer after each traversal, and r_T is the number of recycled pulses that hit the detector. Here we have ignored optical losses and detector inefficiencies for clarity. The power collected at the detector after a single traversal is ηP and the SNR scales as $\sqrt{P_d}$, so the net SNR gain factor will be,

$$\sqrt{\frac{P_d}{\eta P}} = \sqrt{\frac{1 - (1 - \eta)^{r_T}}{\eta}}. \quad (2)$$

For a small post-selection probability—such as those used in weak value experiments—then we can expand (2) around $\eta = 0$ to find,

$$\sqrt{\frac{P_d}{\eta P}} \approx \sqrt{r_T} \left(1 - (r_T - 1) \frac{\eta}{4} \right) + O(\eta^2). \quad (3)$$

For $\eta(r_T - 1) \ll 1$, then we can neglect the attenuation of the pulse to see an approximate $\sqrt{r_T}$ SNR scaling.

For sufficiently large r_T , however, the factor (2) saturates to the constant value $\sqrt{1/\eta}$. This saturation stems from the progressive attenuation of the recycled pulse. Furthermore, the smaller the post-selection probability gets, the larger we can make the possible SNR gain over a single pass. In this limit, however, $P_d \rightarrow P$ according to (1) and all the photons will be collected. Note that despite the large gain in power (2) at the detector, the best SNR that one can obtain still scales according to the standard quantum limit.

The measured signal at the detector may be additionally modified by geometric and propagation effects, which we can encapsulate by an overall factor $\xi(r_T)$ that depends on r_T . The total SNR gain factor over an unrecycled pulse will then be $\xi(r_T) \sqrt{P_d / \eta P}$. For the sake of comparison, we will initially ignore these effects on the signal, so we will approximate $\xi(r_T) \approx 1$ in our qualitative arguments. We will see in subsection IB that for a collimated beam $\xi(r_T)$ will approximate unity for small r_T but will eventually converge to zero for large r_T . Corrections to this effect will be discussed in subsections IB 2d and IB 2e, where we will see that one can maintain a measurable signal for a collimated beam by inverting photons about the optical axis on each traversal or Zeno-stabilizing the beam with a spatial filter. We shall also see in subsection IC that $\xi(r_T)$ can exceed unity for a carefully chosen pulse divergence, which can compensate for the attenuation effects and recover the approximate $\sqrt{r_T}$ scaling for a much wider range of r_T .

3. Recycled Pulse Number

We can compute the number of pulses r_T that hit the detector per laser repetition period T from two factors. First, each trapped pulse can traverse the interferometer roughly $r \leq T/T_r$ times each repetition period. Each traversal contributes one additional pulse impact to the detector. Second, one can accumulate a maximum of $p \leq T_r/T_p = T_r/(\tau + T_g)$ pulses that are trapped inside the interferometer. Hence the total number of detector impacts $r_T = pr$ per period T will be bounded by $T/(\tau + T_g)$. Correspondingly, the maximum SNR gain factor (2) that we can expect from power considerations will also be bounded entirely by the relative time scales and the post-selection probability.

In practice, not every recycled pulse will contribute constructively to the SNR. Indeed, as shown in (2) and as we shall see in subsection IB, there will be some maximum number r_{\max} of constructive pulse impacts before the SNR saturates or decays. To maximize the SNR gain in such a case, the pulse should be discarded and replaced by a fresh pulse. Hence, the number of practical detector collections r_T will be less than the maximum estimation $r_T = pr_{\max} \leq T/(\tau + T_g)$, so the number of pulses p that can fit inside the interferometer will become important. Both pulse stabilization techniques and diverging lenses can increase the practical range of r_{\max} , which we will discuss in subsections IB 2d, IB 2e and IC.

4. Practical Estimates

Using the Pockels cell as a gate, we expect $T_g \approx 2$ ns. Assuming a short pulse $\tau \ll T_g$, then the inter-pulse spacing will be $T_p c \approx T_g c = 0.6$ m. It follows that the maximum number of pulses inside the interferometer will be $p \approx T_r/T_g$. Assuming a large 3m setup, $T_r \approx 10$ ns, so $p \approx 10/2 = 5$ will be a generous upper bound to the number of pulses that we can expect to fit inside any interferometer. For contrast, the smallest setup that fits only a single pulse will be $T_r = T_p$, or $T_p c \approx 0.6$ m in length.

As shown in subsection IB 2c, without loss or stabilization we can expect $r_{\max} \leq 80$ to be an optimistic upper bound for a constructive number of recycling passes. The maximum number of pulse impacts $r_T = pr_{\max}$ per period T that we expect with the largest setup of $p = 5$ pulses is thus $r_T \leq 400$. Therefore, we can expect an SNR gain to span the range from a maximum of $\sqrt{400} = 20$ over a single pass for very small post-selection probability η to $\sqrt{1/\eta}$ for larger η according to (2). Since $r_{\max} \leq T/T_r$ and $T_r \approx 10$ ns for the 3 m setup, the laser repetition period must be $T \approx 400$ ns, implying a repetition rate of $f \approx 2.5$ MHz. For contrast, the smallest setup of 0.6m can fit only $p = 1$ pulse, so $r_T \leq 80$. The SNR gain thus ranges from a maximum of $\sqrt{80} \approx 9$ over a single pass to $\sqrt{1/\eta}$. The 0.6 m setup has recycling period $T_r \approx 2$ ns, so must have a laser repetition period $T \leq 160$ ns, or rate $f \geq 6.25$ MHz. These laser specifications should be readily achievable in the laboratory.

B. Analytic Results

1. Sagnac Interferometer

Following the experiment described in [5, 9, 18], we extend the schematic to pulsed laser operation and pulse recycling. As shown in Fig. 1, the addition of a Pockels cell (PC) and polarizing beam splitter (PBS) allows the unused portion of each pulse that exits the bright port of the Sagnac interferometer to be redirected back inside the interferometer to complete multiple traversals. The combination of half-wave plate (HWP) and Soleil-Babinet compensator (SBC) provide a tunable relative phase ϕ between the clockwise (\odot) and counter-clockwise (\ominus) propagating paths of the interferometer, but also flips the net polarization of each pulse. As a result, the PC must be active as each pulse initially enters the bright port and when each pulse exits the bright port again; however, it must be *inactive* as each pulse returns to the bright port after being confined by the PBS and mirror. By injecting new pulses exactly when older pulses exit the bright port, one can minimize the inter-pulse spacing inside the interferometer to roughly a single gating time.

We also briefly note that the HWP and SBC can be removed in favor of a vertical tilt to provide the relative phase ϕ . With this variation, the PC turns on and off only once per repetition period in order to inject a new pulse into the interferometer, as opposed to cycling for every pulse traversal. This variation does not change the inter-pulse spacing inside the interferometer, however, so it provides no SNR benefits, though it does provide a technical advantage due to the minimized number of PC cycles per laser repetition period T .

2. Pulse Recycling

Because there is no important interaction between distinct pulses in the recycling scheme, the SNR gains are fundamentally determined by the effects of single pulse recycling. Therefore, we shall consider in some detail what happens to a single pulse profile after r passes through the interferometer under the assumption that the pulse remains collimated. We will relax the collimation assumption numerically in subsection IC.

a. Pulse States. Assume the clockwise-propagating state of the pulse in the Sagnac interferometer is denoted $|\odot\rangle$ and the counter-clockwise-propagating state is denoted $|\ominus\rangle$. Then the state that enters the interferometer through the 50:50 beam splitter will have the form, $|\psi_+\rangle = \frac{1}{\sqrt{2}}(|\odot\rangle + i|\ominus\rangle)$. This will also be the post-selection state for the bright port of the interferometer. Similarly, the post-selection state for the dark port of the interferometer will have the orthogonal form, $|\psi_-\rangle = \frac{1}{\sqrt{2}}(|\odot\rangle - i|\ominus\rangle)$. We also define the which-path operator as $\hat{W} = |\odot\rangle\langle\odot| - |\ominus\rangle\langle\ominus|$.

Assume the initial transverse pulse profile is given by a state $|\varphi\rangle$. We normalize the state of the transverse pulse profile so that its squared norm will encode the average photodetection rate. Hence, measuring a pulse with a detector for the pulse duration τ will produce $N = \tau||\varphi||^2$ photon impacts upon the detector per pulse on average. This choice of normalization will allow simple computation of the SNR without multi-particle Fock space calculations (e.g., as used in [21]).

The total initial pulse state that enters the interferometer will have the product form, $|\Psi_0\rangle = |\psi_+\rangle|\varphi\rangle$. For simplicity we suppress the polarization of the state and any propagation effects.

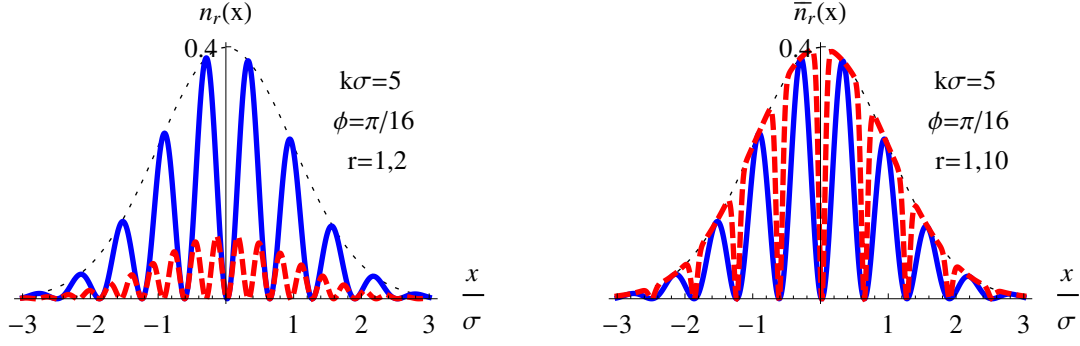


FIG. 2. Strongly misaligned regime with $\phi < 1 < k\sigma$. Left: the transverse pulse profile $n_r(x)$ that impacts the dark port detector on the first (blue, solid) and second (red, dashed) traversals. Right: the accumulated transverse pulse profile $\bar{n}_r(x)$ on the dark port detector after a single (blue, solid) and ten (red, dashed) traversals. For this regime the interference pattern covers the entire profile, subsequent pulses are strongly attenuated, and the interference of the accumulated profile is slowly filled in.

The traversal through the interferometer performs three operations on the state. The first is the passage through the SBC and HWP, which creates a relative phase shift ϕ between the paths that can be described by the unitary operator $\hat{U}_{\text{SBC}} = e^{i\phi\hat{\mathbf{W}}/2}$. The second is the tilting piezo mirror, which imparts a transverse momentum kick k to the pulse, described by the unitary operator $\hat{U}_{\text{P}} = e^{-ik\hat{\mathbf{W}}\hat{\mathbf{x}}}$, where $\hbar = 1$ and the transverse position operator $\hat{\mathbf{x}}$ generates a momentum translation k . The third is a generic uniform loss with probability γ , described by a nonunitary loss operator, $\hat{\mathbf{L}} = \sqrt{1-\gamma}\hat{\mathbf{1}}$.

The state of the pulse profile as it arrives back at the 50:50 beam splitter after one traversal has the form, $|\Psi_1\rangle = \hat{\mathbf{L}}\hat{U}_{\text{P}}\hat{U}_{\text{SBC}}|\Psi_0\rangle$. After the pulse traverses the 50:50 beam splitter, it splits into two paths once more. The dark port projects the photon onto the $|\psi_-\rangle$ state, and the bright port projects the photon onto the $|\psi_+\rangle$ state. Hence, we obtain the following two states in the bright and dark ports, respectively, $|\Psi_{\pm}\rangle = |\psi_{\pm}\rangle \left(\hat{\mathbf{M}}_{\pm}|\varphi\rangle \right)$, where we have factored out the measurement operators $\hat{\mathbf{M}}_{\pm} = \langle\psi_{\pm}|\hat{\mathbf{L}}\hat{U}_{\text{P}}\hat{U}_{\text{SBC}}|\psi_{\pm}\rangle$ that affect the transverse profile of the pulse in each case. Written out explicitly, these measurement operators are diagonal in the position basis and have a remarkably simple form,

$$\hat{\mathbf{M}}_+ = \sqrt{1-\gamma} \cos(\phi/2 - k\hat{\mathbf{x}}), \quad (4a)$$

$$\hat{\mathbf{M}}_- = i\sqrt{1-\gamma} \sin(\phi/2 - k\hat{\mathbf{x}}), \quad (4b)$$

where we have used $\langle\psi_{\pm}|\hat{\mathbf{W}}^n|\psi_{\pm}\rangle = (1 \pm (-1)^n)/2$.

b. Number Densities. Using the measurement operators (4), the exact pulse state that exits the dark port after r traversals through the interferometer will be $|\Psi_-^r\rangle = |\psi_-\rangle \left(\hat{\mathbf{M}}_- (\hat{\mathbf{M}}_+)^{r-1} |\varphi\rangle \right)$. Therefore, the number density $n_r(x)$ of photons that hit the dark port detector at a transverse position x on the r^{th} pulse traversal is,

$$n_r(x) = \tau |\langle x | \Psi_-^r \rangle|^2 = n_0(x) (1-\gamma)^r \times \sin^2 \left(\frac{\phi}{2} - kx \right) \cos^{2(r-1)} \left(\frac{\phi}{2} - kx \right), \quad (5)$$

where $n_0(x) = \tau |\langle x | \varphi \rangle|^2$ is the number density for the input pulse.

The total number density $\bar{n}_r(x)$ that accumulates on the dark port detector after r traversals of the pulse will be the sum of the number densities for the r traversals,

$$\begin{aligned} \bar{n}_r(x) &= \sum_{j=1}^r n_j(x) \\ &= n_0(x) \frac{(1-\gamma) \left(1 - [(1-\gamma) \cos^2(\phi/2 - kx)]^r \right)}{1 + \gamma \cot^2(\phi/2 - kx)}. \end{aligned} \quad (6)$$

Hence the total number of photons that hit the detector after r traversals is $N_r = \int dx \bar{n}_r(x)$. Furthermore, if we compare (6) to the heuristically estimated detector power (1) when $\gamma \rightarrow 0$, we see that the spatially resolved version of the post-selection probability is given by $\eta \leftrightarrow \sin^2(\phi/2 - kx)$.

In the limit of an infinite number of trials $r \rightarrow \infty$, the final term in (6) vanishes and we are left with the number density,

$$\bar{n}_\infty(x) = n_0(x) \frac{1 - \gamma}{1 + \gamma \cot^2(\phi/2 - kx)}. \quad (7)$$

For no loss, $\gamma \rightarrow 0$, the modulating factor from the measurement cancels and the original pulse is *completely recovered*, which is surprising since for the first pass there is an anomalously large position shift. This means that if all the photons in a perfectly collimated pulse are collected through repeated recycling, then the information about the measurement will be erased due to a progressive smearing—or walk-off—effect of the interference pattern, as illustrated in Figs. 2, 3, and 4. Such a result indicates that a collimated pulse should be thrown away or reshaped after a finite number of traversals in order to maximize the information collected at the detector regarding the momentum kick k and the induced phase shift ϕ .

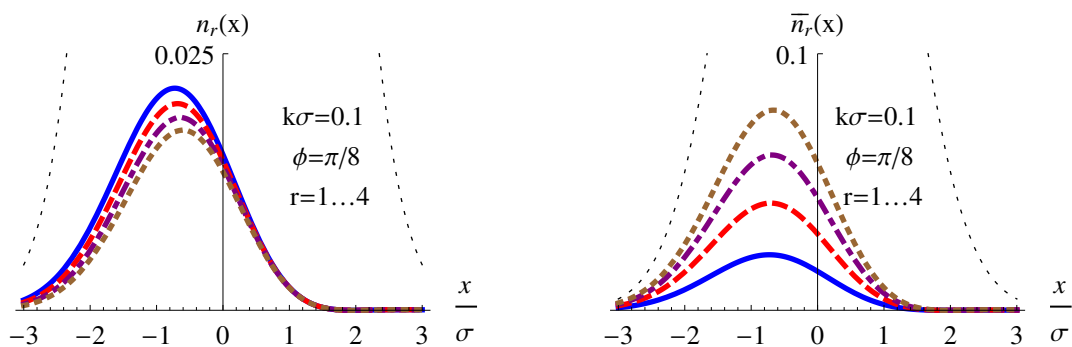


FIG. 3. Weak-value regime with $k\sigma < \phi < 1$, with parameters chosen to exaggerate the walk-off effect. Left: the transverse single-lobed pulse profile $n_r(x)$ that impacts the dark port detector on the first four traversals in order of (blue, solid), (red, dashed), (purple, dot-dashed), and (brown, dotted). Right: the accumulated transverse pulse profile $\bar{n}_r(x)$ on the dark port detector after the first four traversals, with the same color coding. For this regime, the dark port profile resembles a single shifted Gaussian that gradually walks back toward the center on multiple traversals with some attenuation, eventually recovering the original profile. For more realistic parameters, such as those used in [5], the walk-off effect is smaller per traversal.

c. Gaussian Pulse. To gain some intuition about the collected number density (6), consider an initial pulse with a zero-mean Gaussian transverse profile.

$$n_0(x) = \frac{N}{\sqrt{2\pi}\sigma} e^{-x^2/2\sigma^2}. \quad (8)$$

In what follows, we will consider three specific parameter regimes for the Gaussian pulse:

1. the strongly misaligned regime $\phi < 1 < k\sigma$
2. the weak-value regime $k\sigma < \phi < 1$
3. the inverse weak-value regime $\phi < k\sigma < 1$

These regimes are illustrated in Figures 2, 3, and 4, respectively.

In the strongly misaligned regime $\phi < 1 < k\sigma$, the profile that exits the dark port on each traversal (5) is shown in Fig. 2. The interference pattern covers the entire beam profile. On the first pass, the intensity of the peaks match the maximum intensity of the beam. Subsequent passes are strongly attenuated due to the small overlap with the complementary interference pattern in the beam that remains inside the interferometer. The accumulated profile $\bar{n}_r(x)$ in (6) steadily shrinks the width of the interference dips with increasing traversal number until the entire beam profile is recovered. The strongly misaligned regime is unlikely to be useful in a precision measurement due to the large value of k ; we have included it in our discussion for completeness and to emphasize that the single and double lobes that appear in the other regimes are not simple beam shifts, but appear from an interference effect.

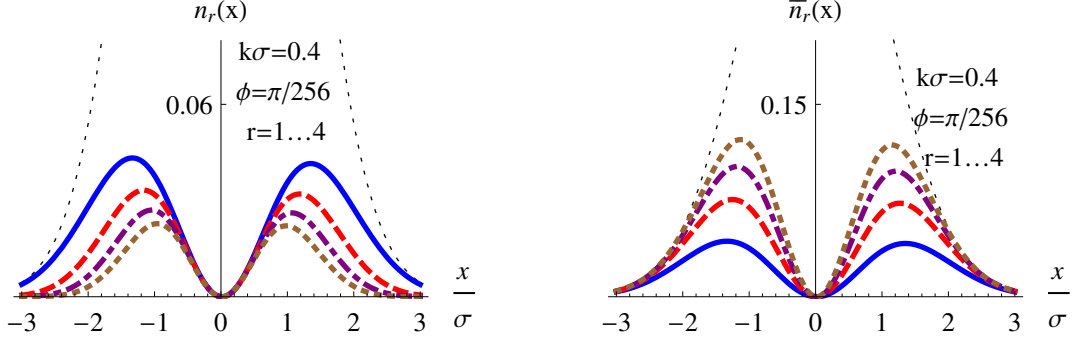


FIG. 4. Inverse weak-value regime with $\phi < k\sigma < 1$, with parameters chosen to exaggerate the walk-off effect. Left: the transverse double-lobed pulse profile $n_r(x)$ that impacts the dark port detector on the first four traversals in order of (blue, solid), (red, dashed), (purple, dot-dashed), and (brown, dotted). Right: the accumulated transverse pulse profile $\bar{n}_r(x)$ on the dark port detector after the first four traversals, with the same color coding. For this regime, there are two lobes that very gradually walk back toward the center on multiple traversals with some attenuation to eventually recover the original beam profile. For more realistic parameters, such as those used in [12, 13], the walk-off effect is smaller per traversal.

For $k\sigma < \phi < 1$, we obtain the weak-value parameter regime considered in [5]. The interference pattern in the number density $n_r(x)$ indicated in (5) leaves a single displaced peak that resembles a shifted Gaussian that is shown in Fig. 3. Subsequent traversals have similar intensities, but progressively walk toward the center with increasing r . The amplified signal comes from the anomalously large shift, so this walk-off degrades the amplification properties of the setup with increasing r .

The walk-off effect arises because the beam that remains inside the interferometer has had a small fraction of light removed by the post-selection from one side, which causes a complementary displacement in the opposing direction. This complementary shift counter-acts the dark-port displacement on subsequent traversals, which makes the output walk back toward the center of the original profile. Hence, after r traversals the accumulated weak-value signal $\bar{n}_r(x)$ (6) will resemble r times the intensity of a single traversal, but will also be degraded due to the walk-off effect. The walk-off is shown exaggerated in Fig. 3, but is a smaller effect per traversal with more realistic parameters, such as those in [5]. However, even though the effect per traversal is smaller, for a sufficiently large number of traversals the signal will always be completely erased by this walk-off effect according to (7).

For $\phi < k\sigma < 1$, we enter the inverse weak-value regime considered in [12, 13] and originally observed in [2]. The weak-value assumptions that produce the single peak break down and (5) produces the double-lobed profile shown in Fig. 4. On multiple traversals the peaks gradually walk back toward the center, similarly to the weak-value regime. However, the forced zero in the center will stabilize the profile, so that after r traversals the accumulated profile $\bar{n}_r(x)$ (6) will more closely resemble r times the intensity of a single traversal than in the weak-value regime. The walk-off is shown exaggerated in Fig. 4, but is also a smaller effect per traversal with more realistic parameters, such as those used in [12, 13].

These different regimes for weak value amplification measurements are also carefully explored in the recent review paper [28].

d. Parity Flips. A simple technique for compensating for the profile erosion on multiple traversals is to invert the profile around the $x = 0$ line so that each new traversal partially cancels the walk-off from the previous traversal. This can be accomplished by introducing a parity-flipping optic represented by a parity operator \hat{P}_x that modifies the profile by replacing $x \rightarrow -x$. This results in a net replacement of the operator $\hat{M}_+ \rightarrow \hat{P}_x \hat{M}_+$ in (4). After an *even* number of traversals $2r$, the accumulated number density (6) then has the modified form,

$$\bar{n}_{2r}(x) = n_0(x) \sin^2 \left(\frac{\phi}{2} - kx \right) \left(1 + \cos^2 \left(\frac{\phi}{2} - kx \right) \right) \times \frac{1 - \left[\cos^2 \left(\frac{\phi}{2} - kx \right) \cos^2 \left(\frac{\phi}{2} + kx \right) \right]^r}{1 - \cos^2 \left(\frac{\phi}{2} - kx \right) \cos^2 \left(\frac{\phi}{2} + kx \right)}, \quad (9)$$

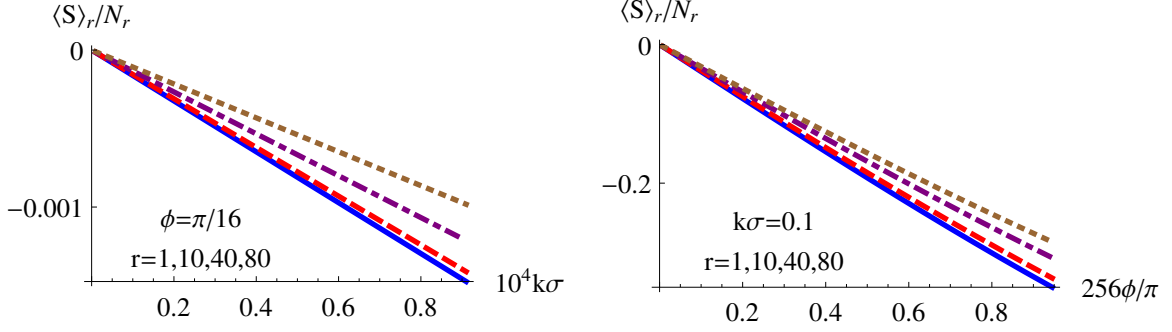


FIG. 5. Normalized split-detection response for a collimated pulse. Left: response for the weak-value regime as a function of $k\sigma$ with fixed ϕ , where $k\sigma < \phi < 1$, and with parameters consistent with Ref. [5]. The accumulated signal is shown for traversal numbers $r = 1$ (blue, solid), $r = 5$ (red, dashed), $r = 10$ (purple, dot-dashed), and $r = 20$ (brown, dotted). Right: response for the inverse weak-value regime as a function of ϕ/π with fixed k , where $\phi < k\sigma < 1$, and with parameters consistent with Ref. [12, 13]. The accumulated signal is shown for the same traversal numbers and color coding. Though the walk-off effects at large traversal numbers change the slope in both regimes, the linear response is preserved. Hence, one can calibrate the slope through repeated experiments with a fixed number of traversals per laser period. The slope is negative here since the signal is negative in Eq. (20).

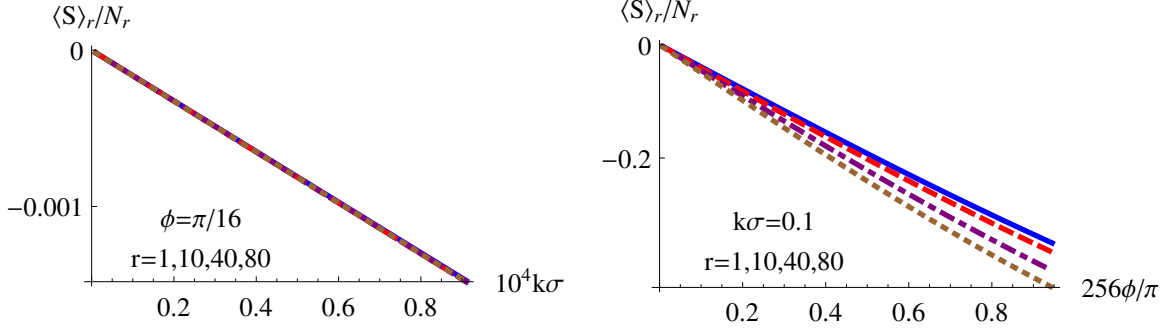


FIG. 6. Normalized split-detection response for a collimated pulse stabilized by parity flipping, using the same color coding as in Figure 5. Left: response for the weak-value regime as a function of $k\sigma$ for fixed ϕ , where $k\sigma < \phi < 1$. All traversal numbers r have the same linear response due to the parity-flip stabilization; Zeno stabilization produces the same result. Right: response for the inverse weak-value regime as a function of ϕ/π for fixed k , where $\phi < k\sigma < 1$. The linear response acquires a steeper slope for larger traversal number using parity-flip stabilization; Zeno stabilization, however, would result in identical slopes for any r .

where we have set $\gamma \rightarrow 0$ for clarity. Unlike (6) where we do not flip the output of the bright port on each traversal, this expression does not yield the original input profile in the limit of large r . Instead it yields,

$$\bar{n}_\infty(x) = n_0(x) \frac{\sin^2\left(\frac{\phi}{2} - kx\right) \left(1 + \cos^2\left(\frac{\phi}{2} - kx\right)\right)}{1 - \cos^2\left(\frac{\phi}{2} - kx\right) \cos^2\left(\frac{\phi}{2} + kx\right)}, \quad (10)$$

which maintains a signal, in contrast with the case of no parity flips on a collimated beam.

e. Zeno stabilization. Another way to reduce transverse walk-off effects and thereby restore the SNR to the power-limited scaling of (2) in subsection IA 2 is to utilize the physics of the quantum Zeno effect by using an optical filter to project the transverse profile back into its original state. The advantage of the Zeno stabilization over parity flipping is that the former does not swap the transverse locations of the photons; this may be important when using quantum states of light, e.g., squeezed or entangled states, whose benefits rely on maintaining transverse correlations between the photons.

At every round of the recycling with Zeno stabilization, the beam is passed through a spatial filter, so if the beam is in its original profile, it will pass through the filter perfectly; however, if the waveform is distorted, then a photon in that mode will have some probability to be absorbed. In passing through the filter on each traversal, a photon in this mode will only experience a small disturbance to the transverse profile, and the state will tend to “freeze” in its original state with only a small rate of being projected into an orthogonal state (in this case, being absorbed by the filter). We note this technique will work regardless of the nature of the disturbance, provided it is small in each pass.

To see how this works, let us consider the Gaussian transverse state in (8) for a single photon ($N = 1$). The corresponding transverse spatial state for this photon has the form

$$\phi_0(x) = \langle x | \phi_0 \rangle = \frac{1}{(2\pi\sigma^2)^{1/4}} \exp\left(-\frac{x^2}{4\sigma^2}\right). \quad (11)$$

After one traversal through the interferometer, the state emerging from the bright port according to (4) is

$$|\phi_1\rangle = \hat{\mathbf{M}}_+ |\phi_0\rangle = \sqrt{1-\gamma} \cos(\phi/2 - k\hat{x}) |\phi_0\rangle. \quad (12)$$

To compute the reshaping probability, we renormalize this state by dividing out its norm

$$\begin{aligned} \langle \phi_1 | \phi_1 \rangle &= (1-\gamma) \int dx |\phi_0(x)|^2 \cos^2(\phi/2 - kx) \\ &= (1-\gamma)(1 + e^{-2k^2\sigma^2} \cos \phi)/2, \end{aligned} \quad (13)$$

to produce the normalized state $|\phi_{1,n}\rangle = |\phi_1\rangle / \sqrt{\langle \phi_1 | \phi_1 \rangle}$.

If we now make a projective measurement with a spatial filter of the shape $|\langle x | \phi_0 \rangle|^2$, the photon will be restored to the state $|\phi_0\rangle$ with a probability $P_1 = |\langle \phi_0 | \phi_{1,n} \rangle|^2$. The probability can be calculated from

$$\begin{aligned} \langle \phi_0 | \phi_{1,n} \rangle &= \frac{1}{\sqrt{N_1}} \int dx |\phi_0(x)|^2 \cos(\phi/2 - kx), \\ &= \frac{\sqrt{2}e^{-k^2\sigma^2/2} \cos(\phi/2)}{\sqrt{1 + e^{-2k^2\sigma^2} \cos \phi}}. \end{aligned} \quad (14)$$

We are interested in the case where both ϕ and $k\sigma$ are less than 1. Consequently, we can expand P_1 to leading order in $k\sigma$ and ϕ ,

$$P_1 = 1 - (k\sigma)^4/2 - (k\sigma)^2\phi^2/4 + \dots, \quad (15)$$

where we drop terms of higher order in powers of $(k\sigma)^2$ and ϕ^2 . In the weak-value regime where $k\sigma < \phi < 1$, the second term in (15) may be dropped. In the inverse weak-value regime where $\phi < k\sigma < 1$, the third term in (15) may be dropped. In either case, for repeated cycles consisting of M independent measurements the probability $P_M = P_1^M$ of being projected back into state $\langle x | \phi_0 \rangle$ will decay approximately exponentially as

$$P_M = \exp[-M\Gamma], \quad (16)$$

where $\Gamma \approx (k\sigma)^4/2 + (k\sigma)^2\phi^2/4$ is an effective decay rate. We can therefore make $M \sim M_Z = 1/\Gamma$ measurements before a photon is typically absorbed by the reshaping filter. This is the manifestation of the Zeno effect, where by making repeated projections, the state is kept in its initial state for much longer than would happen otherwise.

This Zeno number M_Z is many more cycles that we will be able to make before the detector measures all the photons exiting the dark port. For example, if we chose the exaggerated values $k\sigma = 0.1$ and $\phi = \pi/8$ as in Figure 3 then this gives a Zeno number of $M_Z \approx 2.3 \times 10^3$, which is still an order of magnitude larger than we require for the detection physics.

3. Split-detected signal

In order to measure the transverse momentum kick k or the phase shift ϕ we compare the sides of the transverse profile using a split detector. As outlined in subsection IA 2, the accumulated split-detected signal after r pulse repetitions of time duration τ is given by the difference of the number densities on each side,

$$\langle S \rangle_r = \int_0^\infty dx \bar{n}_r(x) - \int_{-\infty}^0 dx \bar{n}_r(x). \quad (17)$$

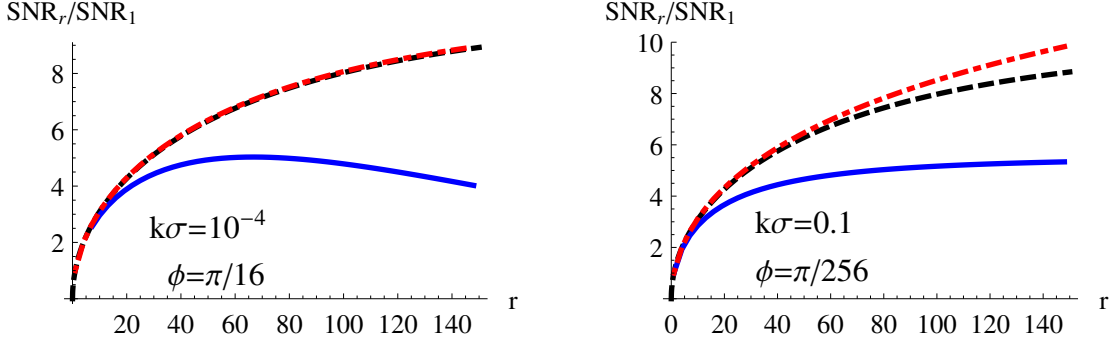


FIG. 7. SNR gain versus traversal number r for a collimated pulse. Left: the SNR gain for the weak-value regime $k\sigma < \phi < 1$ with $k\sigma = 10^{-4}$ and $\phi = \pi/16$. The uncorrected beam with walkoff (blue, solid) shows clear degradation with traversal number, while the beam corrected with parity flipping (red, dashed) as in Sec. I B 2 d matches the simple power scaling law exactly (black, dashed) from Eq. (2). Note that Zeno stabilization will identically produce this power-scaled SNR by construction. Right: the SNR gain for the inverse weak-value regime $\phi < k\sigma < 1$ with $k\sigma = 0.1$ and $\phi = \pi/256$. The uncorrected double-lobed beam with walkoff (blue, solid) shows somewhat less degradation than the weak-value regime due to the forced zero in the profile; however, the double-lobed beam corrected with parity flipping (red, dashed) manages to exceed the simple power scaling law (black, dashed), and thus the scheme with Zeno stabilization.

To measure the displacement of the pulse, the signal should be subsequently normalized by the total photon number $\langle S \rangle_r / N_r$ in order to extract the averaged behavior.

For small displacements the variance of the raw split detected signal is the second moment to a good approximation,

$$(\Delta S)_r^2 \approx \langle S^2 \rangle_r = \int dx \bar{n}_r(x) = N_r, \quad (18)$$

which is the total number of photons that have impacted at the dark port detector. Hence, the SNR that has accumulated after the r^{th} traversal will be given by,

$$\text{SNR}_r = \frac{\langle S \rangle_r}{(\Delta S)_r} = \frac{\langle S \rangle_r}{\sqrt{N_r}}. \quad (19)$$

For the zero-mean Gaussian (8) these quantities can be computed exactly for the first traversal,

$$N_1 = \frac{(1-\gamma)N}{2} \left(1 - e^{-(2k\sigma)^2/2} \cos \phi \right), \quad (20a)$$

$$\langle S \rangle_1 = -\frac{(1-\gamma)N}{2} e^{-(2k\sigma)^2/2} \text{Erfi}(\sqrt{2}k\sigma) \sin \phi, \quad (20b)$$

$$\frac{\langle S \rangle_1}{N_1} = -\text{Erfi}(\sqrt{2}k\sigma) \frac{e^{-(2k\sigma)^2/2} \sin \phi}{1 - e^{-(2k\sigma)^2/2} \cos \phi}, \quad (20c)$$

$$\text{SNR}_1 = -\sqrt{(1-\gamma)N} \frac{\text{Erfi}(\sqrt{2}k\sigma) e^{-(2k\sigma)^2/2} \sin \phi}{\sqrt{2(1 - e^{-(2k\sigma)^2/2} \cos \phi)}}, \quad (20d)$$

where $\text{Erfi}(x) = \text{Erf}(ix)/i = (2/\sqrt{\pi}) \int_0^x e^{t^2} dt$ is the imaginary error function. We now specialize these exact solutions to the two amplification regimes under consideration and indicate numerically how larger traversal numbers behave in each regime.

a. Weak-value regime. When $k\sigma < \phi < 1$ then we can neglect terms of order $(k\sigma)^2$ in (20) to find,

$$N_1 = (1-\gamma)N \sin^2(\phi/2), \quad (21a)$$

$$\langle S \rangle_1 = -\sqrt{\frac{2}{\pi}} (1-\gamma)N k\sigma \sin \phi, \quad (21b)$$

$$\frac{\langle S \rangle_1}{N_1} = -\sqrt{\frac{2}{\pi}} 2k\sigma \cot(\phi/2), \quad (21c)$$

$$\begin{aligned} \text{SNR}_1 &= -\sqrt{\frac{2}{\pi}} \sqrt{(1-\gamma)N} (2k\sigma \cos(\phi/2)) \\ &= -\sqrt{\frac{2}{\pi}} \sqrt{N_1} (2k\sigma \cot(\phi/2)). \end{aligned} \quad (21d)$$

These linear order solutions correctly match the weak value analyses made in [5, 9, 18], as expected. Due to the factor $\cot(\phi/2)$ in the normalized split detection $\langle S \rangle_1/N_1$, setting a known small ϕ provides an amplification factor for measuring an unknown small k . This regime gets its name from the fact that this amplification factor is the imaginary part of the weak value $W_w = \langle \psi_- | \hat{\mathbf{W}} | \psi_\phi \rangle / \langle \psi_- | \psi_\phi \rangle = i \cot(\phi/2)$ of the which-path operator $\hat{\mathbf{W}}$ with initial state $|\psi_\phi\rangle = \hat{\mathbf{U}}_{\text{SBC}} |\psi_+\rangle$ and post-selection state $|\psi_-\rangle$. The normalized signal for this parameter regime is shown in the left plot of Fig. 5 as a function of $k\sigma$, demonstrating the linear response.

We can reproduce the dominant SNR gain factor for small post-selection probability by neglecting the walk-off effects and the power attenuation. To do this, we expand the accumulate profile $\bar{n}_r(x)$ in (6) to first order in $k\sigma$ and second order in ϕ to obtain,

$$\bar{n}_r(x) = rc(\gamma, r) n_0(x) \left(-kx\phi + \left(\frac{\phi}{2} \right)^2 \right), \quad (22)$$

$$c(\gamma, r) = \frac{(1-\gamma)(1-(1-\gamma)^r)}{r\gamma}, \quad (23)$$

where $\lim_{\gamma \rightarrow 0} c(\gamma, r) = 1$.

The only r -dependence in the number density is in the numeric prefactor $rc(\gamma, r)$, which effectively scales the total photon number $N \rightarrow rc(\gamma, r)N$. Using this scaling, the result (21) for the split-detector will hold for any r to second order in ϕ and first order in k . Hence, the SNR should scale as $\sqrt{Nrc(\gamma, r)}$ when walk-off and power attenuation effects are neglected. When $\gamma \rightarrow 0$, this recovers the dominant \sqrt{r} SNR enhancement factor that we found to zeroth order in the post-selection probability of (2) in subsection IA 2 from power considerations.

However, the walk-off effects and power attenuation combine to reduce the actual SNR below this optimistic level. To see this, consider the solid blue curve in the left plot of Fig. 7, which shows the split-detected SNR gain versus traversal number for the weak-value regime. The SNR gain for any sufficiently small $k\sigma$ is universal, but plateaus quickly due to the beam degradation from the walk-off. Even worse, for sufficiently large traversal number r the signal will eventually decline and then converge to zero due to the erasure effect implied by (7), so the SNR gain factor will also correspondingly decay to zero.

The power scaling in (2) can be recovered, however, if the walk-off is corrected with the parity flipping method discussed in subsection IB 2d. The normalized signal produced with the parity-flip correction—illustrated in the left plot of Fig. 6—has an identical slope for any traversal number, demonstrating the simple power scaling behavior. This correction is illustrated as the dot-dashed red curve in the left plot of Fig. 7, which exactly overlaps the power scaling curve illustrated as the dashed black curve. If the walk-off is corrected with Zeno stabilization instead, then the signal slope will be identical for any traversal number by construction, and the SNR gain will also exactly follow the power scaling curve in (2).

b. Inverse weak-value regime. If $\phi < k\sigma < 1$, then the approximation to linear order in $k\sigma$ will break down, as shown earlier in subsection IB 2c. For this regime, we keep linear order in ϕ and second order in $k\sigma$ in (20) to find,

$$N_1 = (1-\gamma)N(k\sigma)^2, \quad (24a)$$

$$\langle S \rangle_1 = -\sqrt{\frac{2}{\pi}} (1-\gamma) N k \sigma \phi, \quad (24b)$$

$$\frac{\langle S \rangle_1}{N_1} = \sqrt{\frac{2}{\pi}} \left(\frac{k\sigma}{3} - \frac{1}{k\sigma} \right) \phi, \quad (24c)$$

$$\begin{aligned} \text{SNR}_1 &= \sqrt{\frac{2}{\pi}} \sqrt{(1-\gamma)N} \left(\frac{5}{6} (k\sigma)^2 - 1 \right) \phi \\ &= \sqrt{\frac{2}{\pi}} \sqrt{N_1} \left(\frac{5}{6} k\sigma - \frac{1}{k\sigma} \right) \phi. \end{aligned} \quad (24d)$$

In contrast to the previous approximation, the $1/k$ term in the normalized signal $\langle S \rangle_1/N_1$ leads to an amplification in measuring an unknown ϕ given a known small k . Indeed, this regime was used in Refs. [12, 13] for exactly this

Symbol	Numerical Value
ℓ	1.5 m
σ	1 mm
k	$1 \times 10^{-3} \text{ m}^{-1}$
k_0	$8 \times 10^6 \text{ m}^{-1}$
γ	0.01
d	1 cm

TABLE II. Parameters used for numerical computations. ℓ is half the length of the interferometer, k is the momentum kick from the mirror, σ is the input beam width, k_0 is the carrier momentum, γ is the loss per traversal, and d is the half-width of the split-detector.

purpose. In the preprint version of Ref. [13] it was noted that $\phi \approx 2\text{Im}W_w^{-1}$ is the inverse of the weak value present in the weak-value regime for small ϕ , which motivates our name for this parameter regime; this inverted relationship has also been rediscovered more recently in Ref. [28]. The normalized signal for this parameter regime is shown in the right plot of Fig. 5 as a function of ϕ , demonstrating the linear response.

Again, we can reproduce the dominant SNR gain factor for small post-selection probability by neglecting the walk-off effects and the power attenuation, which can be done by expanding $\bar{n}_r(x)$ to second order in $k\sigma$ and first order in ϕ to obtain,

$$\bar{n}_r(x) = rc(\gamma, r)n_0(x) (-kx\phi + k^2x^2), \quad (25)$$

with the same $c(\gamma, r)$ as in (23).

As with the weak-value regime, the only r -dependence in the number density is in the numeric prefactor $rc(\gamma, r)$, which effectively scales the total photon number $N \rightarrow rc(\gamma, r)N$. Using this scaling, the result (24) for the split-detector will hold for any r to second order in k and first order in ϕ . Hence, the SNR will scale as $\sqrt{Nrc(\gamma, r)}$ when walk-off and power attenuation effects are neglected. When $\gamma \rightarrow 0$, this also recovers the dominant \sqrt{r} SNR enhancement factor that we found to zeroth order in the post-selection probability of (2) in subsection IA 2 from power considerations.

As before, the walk-off and power attenuation effects reduce the SNR gain below this optimistic level. Consider the solid blue curve in the right plot of Fig. 7, which shows the exact split-detected SNR gain versus traversal number for the inverse weak-value regime. As anticipated in subsection IB 2 c, the forced zero in the center of the double-lobed profile naturally stabilizes the beam to produce a saturated SNR for more traversals than the weak-value regime. However, the SNR still plateaus relatively quickly before eventually decaying to zero for a sufficiently large number of traversals r without additional stabilization.

Similarly, the degradation from walk-off can be completely reversed by employing the parity flipping technique. The dot-dashed red curve in the right plot of Fig. 7 actually *exceeds* the simple power scaling law illustrated as the dashed black curve due to an additional accumulation of momentum information on each subsequent traversal. Moreover, the normalized signal shown in the right plot of Fig. 6 shows a corresponding increase in the slope of SNR vs. ϕ with traversal number.

C. Diverging Pulse

By assuming a collimated beam, we have so far neglected beam propagation effects in the analysis, as well as any lens effects that could further change the detection physics. In order to incorporate these effects, we now alter our measurement operators and pursue a numerical approach. We find that these effects may slightly enhance the SNR gains from recycling before saturation due to the finite detector size, but do not fundamentally alter the basic power-scaling behavior. For that reason, it will be sufficient to illustrate only the weak-value regime as an example.

Extending the collimated analysis in subsection IB to include beam propagation leads to a replacement of the measurement operators with $\hat{M}_\pm \rightarrow \hat{M}'_\pm = \hat{U}_\ell \hat{M}_\pm \hat{U}_\ell$, where $\hat{U}_\ell = \exp(-i\hat{\mathbf{p}}^2\ell/2k_0)$, k_0 is the carrier momentum of the pulse, and ℓ is the propagation length from piezo to 50:50 beam splitter [29]. The number density (5) will then involve the composite measurement operator

$$\hat{M}'_- \left(\hat{M}'_+ \right)^{r-1} = \hat{U}_\ell \hat{M}_- \hat{U}_\ell \left(\hat{U}_\ell \hat{M}_+ \hat{U}_\ell \right)^{r-1}. \quad (26)$$

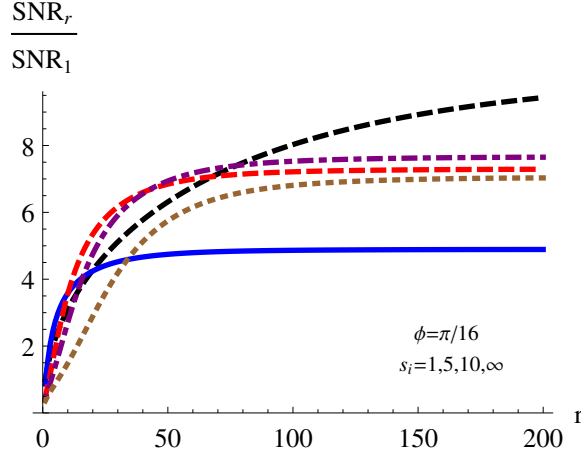


FIG. 8. The effect of propagation and different diverging lens choices on the SNR of the weak-value regime with $k\sigma = 10^{-6}$ and $\phi = \pi/16$. In order of (blue, solid), (red, dashed), (purple, dot-dashed), and (brown, dotted) we show weak initial diverging lenses with extreme focal lengths $s_i = -1$ m, -5 m, -10 m, and no lens. The (black, dashed) curve shows the scaling given by power considerations in Eq. (2). Here SNR_1 refers to the SNR of a single unrecycled pulse with an optimally chosen focal length of $s_i = -0.5$ m, while SNR_r is the accumulated SNR over r traversals for the indicated lens choices.

Adding a diverging lens with focal length s_i also modifies the initial state with an operator $\hat{U}_L = \exp(ik_0\hat{x}^2/2s_i)$. Hence, powers of the following modified operators will appear in the full solution,

$$\hat{U}_\ell \hat{M}_- = ie^{-i\hat{p}^2\ell/2k_0} \sin(\phi/2 - k\hat{x}), \quad (27a)$$

$$\hat{U}_\ell^2 \hat{M}_+ = e^{-i\hat{p}^2\ell/k_0} \cos(\phi/2 - k\hat{x}), \quad (27b)$$

$$\hat{U}_\ell \hat{U}_L = e^{-i\hat{p}^2\ell/2k_0} e^{ik_0\hat{x}^2/2s_i}, \quad (27c)$$

which can be simplified recursively. The effect of a diverging lens is considered for comparison with the unrecycled experiment in Ref. [5], where such a lens was able to enhance sensitivity.

Table II shows the parameters which describe the laser and experimental geometry. Our choice of k_0 corresponds to the 780-800 nm lasers used in [5, 9, 12, 13], and the 3-meter interferometer length ℓ is taken from the generous upper bound estimate discussed in subsection IA as a worst case scenario for beam divergence effects. For the weak-value regime of small $k\sigma$ and ϕ such that $k\sigma < \phi < 1$, we found that it was more computationally efficient to expand the sine and cosine functions in (27) to second order in k and fourth order in ϕ . To test the validity of this truncation, we initially set the interferometer length ℓ to zero so that a comparison could be made with the previously calculated collimated solutions.

We restrict our attention to the SNR gains achieved by recycling a single pulse for r traversals, since adding more pulses leads to a simple scaling of the single pulse result. The SNR gains for different choices of initial diverging lens are shown in Fig. 8, where they are compared to the ideal power-scaling curve that we expect from our qualitative considerations given by (2). In all cases, the expected gains roughly follow the qualitative power scaling rule for a large number of traversals before saturating due to the beam growing larger than the finite size of the split-detector. Note that the beam divergence mitigates the SNR decay that was observed for the collimated case, even without beam stabilization due to flipping or Zeno reshaping.

D. Section Conclusion

By investigating the optical design shown in Fig. 1, we have shown how a single optical pulse can be trapped inside the interferometer until the photons all exit the dark port and are “post-selected,” greatly boosting the sensitivity of the precision measurement. The added power accumulated at the detector within a fixed duration of time is the dominant source of sensitivity gain. Further increases are achievable by trapping multiple pulses in the interferometer simultaneously. The number of trapped pulses is limited by the length of the pulses, the gating frequency of current Pockels cells, and the physical size of the interferometer.

We carefully analyzed the case of a collimated beam and showed that repeated post-selections cause a walk-off effect in the recycled pulse, which tends to diminish the SNR. However, we also showed that these walk-off effects

can be easily corrected by Zeno reshaping, or by a parity flip, which reflects the beam around its optic axis on each traversal. Somewhat surprisingly, the gains with parity correction can even exceed those expected from the power scaling. Including propagation effects does not destroy the sensitivity gain shown for the collimated case, but instead can produce additional enhancement.

While these sensitivity gains alone are a substantial improvement over the original idea, the combination of these techniques with other established metrology techniques—such as the use of a squeezed reference beam—could further increase the sensitivity beyond that indicated here.

II. ANALYSIS OF ADVANTAGES OF WEAK VALUE AMPLIFICATION IN THE PRESENCE OF TECHNICAL NOISE

In the previous section, we demonstrated how the weak value amplification techniques can be further improved by recycling most of the light emerging from the bright port that does not contain information about the desired parameter. Another very important issue relates to how the original (un-recycled) measurement scheme improves the accuracy of precision measurement, and we will now report on our findings, also discussed in Ref. [30]. While we have discovered that these techniques, in and of themselves, do not overcome fundamental limits for coherent light sources (“standard quantum limit”) (see *e.g.* [9]), there are technical advantages in that these methods make the experimental approach to these limits relatively easy with common experimental equipment. Many concrete examples were mentioned in the introduction of this report and will be described in the following sections. Recent results in quantum metrology [31] indicate that under very general conditions, quantum light sources do poorly in the presence of additional noise. Therefore, the fact we demonstrate that the weak value techniques can perform much better than standard coherent state methods in the presence of technical noise is a very exciting prospect for precision measurements.

Although these experimental findings have been employed in a number of different research groups and applied to metrological questions of a number of different physical parameters, there are still some open questions and even controversy [32, 33] about this technique: precisely how and to what extent can WVA techniques help against technical noise, or give some kind of technical advantage in comparison to the standard measurement techniques? Starling *et al.* considered a particular parameter estimator, showing that WVA could give an advantage [9]. An important step was made in this question when Feizpour, Xingxing, and Steinberg [34] were able to consider a more general kind of technical noise, and showed that so long as it had a long correlation time, WVA also help suppress it in the SNR. In other closely related work, Kedem [35], Brunner and Simon [3] and Nishizawa [36] also showed an increased performance of the SNR in the presence of technical noise.

In contrast to these results, recent papers have claimed that WVA gives no technical advantage [32, 33]. The argument is justified by using a Fisher information analysis of technical noise applied to the signal carrier (e.g., such as beam displacement jitter). (We note the Fisher information analysis has been recently applied to WVA by other authors as well [15, 37].) However, this particular form of technical noise does not represent the complete picture. There are many forms of technical noise that are not incorporated in this model. For example, in optical beam deflection, noise sources include: electronics noise, transverse displacement and angular jitter, analog-to-digital discretization noise, turbulence, vibration noise of the other optical elements, spectral jitter, etc. We will analyze some of these models and examples using Fisher information and maximum likelihood methods in order to understand in precisely what sense they give or fail to give a technical advantage, as well as describe other technical advantages in beam deflection (and derivative) experiments where the imaginary WVA technique does lead to the optimal Fisher information even in the presence of some types of noise sources mentioned above.

We organize this section as follows. In Sec. II A, we introduce the concepts of Fisher information and maximum likelihood techniques, and illustrate how to apply them to Gaussian random measurements. We introduce weak value amplification and postselection in Sec. II B. Uncorrelated, displacement technical noise is discussed in Sec. II D. Time correlated technical noise is analyzed in Sec. II E. Air turbulence is discussed briefly in Sec. II F. The combination of displacement jitter and turbulence is discussed in Sec. II G, showing the weak value technique can suppress both. The weak value technique is shown to better suppress angular jitter in deflection measurements in Sec. II H. We examine a recent photon recycling proposal in Sec. II I and show the Fisher information is boosted by the inverse postselection probability. Our conclusions are summarized in Sec. II J.

A. Fisher information of an unknown parameter

Fisher information describes the available information about an unknown parameter in a given probability distribution. Consider an unknown parameter d , upon which some random variable x depends. Let the probability

distribution of x , given d be $p(x|d)$. The score of the distribution is defined as $S = \partial_d \log p(x|d)$. Assuming p is a smooth function, the average of S over p is 0, and its variance (second moment) is defined as the Fisher information,

$$\mathcal{I}(d) = \langle S^2 \rangle = \int dx p(x|d) (\partial_d \log p(x|d))^2 \quad (28)$$

$$= - \int dx p(x|d) \partial_d^2 \log p(x|d). \quad (29)$$

Fisher information is additive over independent trials, so for N statistically independent measurements (such as the collection of N photons from a coherent source), $\mathcal{I}_N(d) = N\mathcal{I}(d)$.

Consider an unbiased estimator of d , called \hat{d} . This is any statistical estimator whose expectation value is d . The variance of \hat{d} is bounded from below by the Cramér-Rao bound (CRB), or $\text{Var}[\hat{d}] \geq \mathcal{I}(d)^{-1}$. Thus, the Fisher information sets the minimal possible estimate on the uncertainty of d , for any unbiased estimator.

To illustrate how this works, let us consider a Gaussian distribution for $p(\{x_i\}|d)$, which will describe N independent measurements $\{x_i\}$ of an unknown mean with known variance σ^2 for each measurement,

$$P_G(\{x_i\}|d) = \prod_{i=1}^N \frac{1}{\sqrt{2\pi\sigma^2}} \exp\left(-\frac{(x_i - d)^2}{2\sigma^2}\right). \quad (30)$$

In this example, the score is given by $S = \sum_{i=1}^N (x_i - d)/\sigma^2$, so indeed $\langle S \rangle = 0$, and the Fisher information is given by

$$\mathcal{I}_G(d) = N\sigma^{-2}. \quad (31)$$

Thus, the CRB on the variance is simply σ^2/N . Consequently, the minimum resolvable signal d_{min} will be of order of $d_{min} \sim \sigma/\sqrt{N}$. In order to achieve this minimum bound on the variance, the optimal unbiased estimator \hat{d}_{opt} (often called the efficient estimator) must be used. We can find it with maximum likelihood methods, by setting the score to zero, and replacing d by \hat{d}_{opt} . In the case of P_G , we have

$$S(d \rightarrow \hat{d}_{opt}) = \sum_{j=1}^N (x_j - \hat{d}_{opt})/\sigma^2 = 0, \quad (32)$$

so we find the efficient estimator,

$$\hat{d}_{opt} = (1/N) \sum_{j=1}^N x_j, \quad (33)$$

which is simply the average of the data in this case. We can check that the variance gives the inverse CRB: $\langle (\hat{d}_{opt} - d)^2 \rangle = (1/N^2) \sum_{i,j} \langle x_i x_j \rangle = \sigma^2/N$. In an optical context, this is the “standard quantum limit” scaling with N , which we can interpret as the photon number. Here the parameter d can be interpreted as the displacement of a beam with transverse width σ . One can immediately see that the maximum Fisher information occurs for the smallest allowable beam waist. This is intuitively obvious. If a beam of very small waist experiences a small shift in its mean value, a position sensitive detector (e.g., a split detector) would see a large change in intensity as a function of its position compared to a beam with a large waist.

In the rest of this report, we will consider coherent Gaussian distributions for simplicity. While this is somewhat restrictive, it is also quite reasonable since most of the experiments have been performed using coherent Gaussian probability densities. This is also quite nice theoretically, owing to the fact that the log likelihood function is twice differentiable and we can use variations of the simple form of the Fisher information derived above.

B. Real weak values and postselection

To apply the above results to recent optical experiments, we briefly recall a few facts about weak values [1]. If a quantum system is prepared in an initial state $|i\rangle$, has a system operator A that is measured by weakly interacting with a meter prepared in a state of spatial variance σ^2 , and then postselected in a final state $|f\rangle$ with probability $\gamma = |\langle f|i \rangle|^2$, the meter degree of freedom will be shifted by a multiplicative factor

$$A_w = \langle f|A|i \rangle / \langle f|i \rangle, \quad (34)$$

where A_w is the weak value of the operator A , while leaving the width σ unchanged (for the moment we consider the real weak value case for simplicity). Such behavior is in contrast to the non-postselected case, where if the initial state is an eigenstate of A , so that $A|i\rangle = a_i|i\rangle$, the average meter shift is a_id , which can be much smaller in size than the weak value shift, $A_w d$.

This process gives rise to a (normalized) Gaussian meter probability distribution consisting of $N' = \gamma N$ measurement events $\{x'_i\}$,

$$P'_G(\{x'_i\}|d) = \prod_{i=1}^{N'} \frac{1}{\sqrt{2\pi\sigma^2}} \exp\left(-\frac{(x'_i - A_w d)^2}{2\sigma^2}\right). \quad (35)$$

Computing the CRB on the variance as before gives the score to be $S = A_w \sum_{i=1}^{N'} (x'_i - A_w d)/\sigma^2$, so the Fisher information is

$$\mathcal{I}_G(d) = (A_w)^2 N' \sigma^{-2} = \langle f|A|i\rangle^2 N \sigma^{-2}. \quad (36)$$

Note that the post-selection probability γ canceled out. Therefore, the Fisher information is the same as before, except for a factor $\langle f|A|i\rangle^2$, a number that can be arranged to approach 1 for a two-level system with a judicious choice of operator, pre- and post-selection (see Sec. II C). This is consistent with the SNR analysis of Ref. [9]. Similar points were made by Hofmann *et al.* [38]. We can then extract all the Fisher information from the weak value, showing that ideally, the WV technique can put all of the Fisher information into the post-selected events, which matches the Fisher information in the standard methods using all of the events. We note that it is not surprising that considering any sub-ensemble gives less information than the whole ensemble. What *is surprising* is that by using this particular small sub-ensemble gives you all the Fisher information. This fact alone gives us technical advantages, as we shall see.

Following the maximum likelihood method presented in Eqs. (32,33), the weak value efficient estimator is given by $\hat{d}_{wv} = (1/A_w N') \sum_{j=1}^{N'} x_i$.

C. Weak value for a two-level system

Our calculations are based on an interaction of the type $U = \exp(-i d \hat{p} \hat{A})$, where d is the unknown small parameter. Tracking/measurements of the meter degree of freedom x after the postselection gives a SNR of $\mathcal{R} = (\sqrt{N} d/\sigma) \times |\langle f|i\rangle \text{Re}(A_w)|$. If instead, measurements of the conjugate momentum p are performed, the result is $\mathcal{R} = (\sqrt{N} d/\sigma) \times |\langle f|i\rangle \text{Im}(A_w)|$ [35]. We will show that under the right choices for pre- and post-selection, $|\langle f|i\rangle \text{Re}(A_w)| = 1$ or $|\langle f|i\rangle \text{Im}(A_w)| = 1$.

We chose to consider the operator \hat{A} such that $\hat{A}|\pm\rangle = \pm|\pm\rangle$, where $|+\rangle$ and $|-\rangle$ form an orthonormal basis for the Hilbert space of a two-level system. The initial state of the system can be written as

$$|i\rangle = \cos\left(\frac{\Theta}{2}\right) |+\rangle + e^{i\Phi} \sin\left(\frac{\Theta}{2}\right) |-\rangle, \quad (37)$$

where $0 < \Theta < \pi$ and $0 < \Phi < 2\pi$ represent the qubit state on the surface of the Bloch sphere. The postselection state for the system is defined as

$$|f\rangle = \sin\left(\frac{\Theta}{2} + \theta\right) |+\rangle - e^{i(\Phi+2\phi)} \cos\left(\frac{\Theta}{2} + \theta\right) |-\rangle, \quad (38)$$

where θ and ϕ are angles representing the deviation (in both angular directions on the Bloch sphere, see Fig. 9) from the state orthogonal to $|i\rangle$.

The probability of the postselection on $|f\rangle$ and the weak value take the form,

$$\gamma \approx |\langle f|i\rangle|^2 = \cos^2 \phi \sin^2 \theta + \sin^2(\Theta + \theta) \sin^2 \phi, \quad (39)$$

$$\text{Re}(A_w) = \frac{\sin \theta \sin(\Theta + \theta)}{|\langle f|i\rangle|^2}, \quad (40)$$

$$\text{Im}(A_w) = -\frac{\sin \Theta \sin(\Theta + 2\theta) \sin(2\phi)}{2|\langle f|i\rangle|^2}. \quad (41)$$

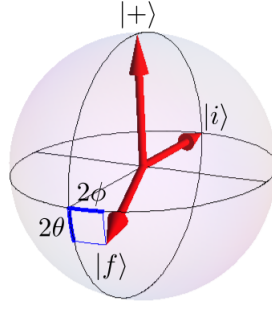


FIG. 9. Representation on the Bloch sphere of the preselection and postselection states for $\Theta = \pi/2$. The state $|i\rangle$ corresponds to a unit vector anywhere on the equatorial plane, and the state $|f\rangle$ is off to be antiparallel to $|i\rangle$ in the two angular directions. The angle 2θ (2ϕ) gives origin to the real (imaginary) part of the weak value.

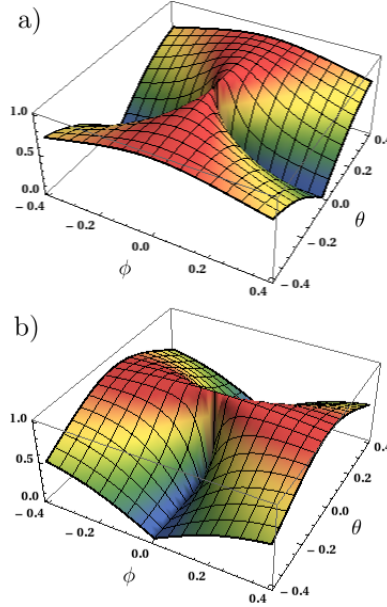


FIG. 10. $|\langle f|i\rangle \text{Re}(A_w)|$ (a) and $|\langle f|i\rangle \text{Im}(A_w)|$ (b) as a function of θ and ϕ , for $\Theta = \pi/2$ (see text for details). Both functions are upper bounded by unity.

Note that the angles θ and ϕ are the respective generators of the real and the imaginary part of the weak value. For example, a pure imaginary weak value can be obtained making $\theta = 0$, so $\gamma = \sin^2 \Theta \sin^2 \phi$ and $A_w = -i \cot \phi$. In order to maximize γ we choose $\Theta = \pi/2$, so the results are $|i\rangle = [|\!+\rangle + e^{i\Phi}|\!-\rangle] / \sqrt{2}$ and $|f\rangle = [e^{-i\phi}|\!+\rangle - e^{i\Phi+i\phi}|\!-\rangle] / \sqrt{2}$. Finally, in the small angle approximation, $\gamma \approx \phi^2$ and $A_w \approx -i/\phi$, making $|\langle f|i\rangle \text{Im}(A_w)| \approx 1$. On the other side, a pure real weak value can be obtained making $\phi = 0$, so $\gamma = \sin^2 \theta$, and $A_w = \sin(\Theta + \theta) / \sin \theta$. In order to make A_w large for this case, we choose again $\Theta = \pi/2$. The preselection is identical to the former case $|i\rangle = [|\!+\rangle + e^{i\Phi}|\!-\rangle] / \sqrt{2}$, and the postselection takes the form $|f\rangle = \sin \theta [|\!+\rangle + e^{i\Phi}|\!-\rangle] / \sqrt{2} + \cos \theta [|\!+\rangle - e^{i\Phi}|\!-\rangle] / \sqrt{2}$. Taking the small angle approximation for this case we obtain a similar result to the pure imaginary weak value case, $\gamma \approx \theta^2$, $A_w \approx 1/\theta$, and $|\langle f|i\rangle \text{Re}(A_w)| \approx 1$.

Setting $\Theta = \pi/2$ turns out to be the best choice for practical purposes. We therefore calculate the products $|\langle f|i\rangle \text{Re}(A_w)|$ and $|\langle f|i\rangle \text{Im}(A_w)|$ for such a choice, and plot them in Fig. 10. It is shown in Fig. 10(a) that the largest value $|\langle f|i\rangle \text{Re}(A_w)| = 1$ is closest reached if $\phi = 0$ and $|\theta| \ll 1$, which corresponds to a pure real weak value and an almost orthogonal postselection. Similarly, Fig. 10(b) shows that $|\langle f|i\rangle \text{Im}(A_w)| \approx 1$ only if $\theta = 0$ and $|\phi| \ll 1$, defining a pure imaginary weak value with almost orthogonal postselection.

D. Type 1 technical noise: Displacement noise

As a next step, we include the effect of one kind of technical noise. We first consider the technical noise model of Knee and Gauger, where the N random variables $\{x_i\}$ are independently distributed with mean d and variance σ^2 [32]. We note that similar models have also been previously discussed in Refs. [9, 34, 35]. Gaussian white technical noise $\{\xi_i\}$ is added to $\{x_i\}$ with mean 0 and covariance $\langle \xi_i \xi_j \rangle = J^2 \delta_{ij}$. Knee and Gauger comment that this kind of noise might represent transverse beam displacement jitter (in a collimated beam), for example. We call this *type 1* technical noise. The measured signal will be the sum of $s_i = x_i + \xi_i$, so the distribution function for s_i is $p(\{s_i\}|d) = \int \mathcal{D}x \mathcal{D}\xi p(\{x_i\})p(\{\xi_i\})\delta(s_i - x_i - \xi_i)$, where $\int \mathcal{D}x = \prod_{i=1}^N \int dx_i$ integrates over all variables. Integrating over x_i gives the distribution of the measured results as a convolution of the two distributions,

$$\begin{aligned} p(\{s_i\}|d) &= \prod_{i=1}^N \int d\xi_i \mathcal{N} \exp\left(-\frac{(d - s_i - \xi_i)^2}{2\sigma^2}\right) e^{-\xi_i^2/2J^2} \\ &= \prod_{i=1}^N \frac{1}{\sqrt{2\pi(\sigma^2 + J^2)}} \exp\left(-\frac{(d - s_i)^2}{2(\sigma^2 + J^2)}\right), \end{aligned} \quad (42)$$

where \mathcal{N} is a normalization constant. Calculating the Fisher information as before, for N independent measurements (photons) gives

$$\mathcal{I}_{KG} = \frac{N}{\sigma^2 + J^2}. \quad (43)$$

The technical noise simply broadens the width, decreasing the Fisher information. In the weak value case, we follow the same procedure, except that $d \rightarrow A_w d$, and $N \rightarrow N' = \gamma N$, where γ is the post-selection probability. We add the same technical noise to the resulting distribution of post-selected events $\{s'_i\}$, and get

$$\begin{aligned} p'(\{s'_i\}|d) &= \prod_{i=1}^{N'} \int d\xi_i \mathcal{N} \exp\left(-\frac{(dA_w - s'_i - \xi_i)^2}{2\sigma^2}\right) e^{-\xi_i^2/2J^2} \\ &= \prod_{i=1}^{N'} \frac{1}{\sqrt{2\pi(\sigma^2 + J^2)}} \exp\left(-\frac{(dA_w - s'_i)^2}{2(\sigma^2 + J^2)}\right). \end{aligned} \quad (44)$$

Calculating the Fisher information for the postselected case (which must be reduced by γ , the post-selection probability) gives

$$\mathcal{I}'_{KG} = \frac{\gamma A_w^2 N}{\sigma^2 + J^2} = \frac{\langle f|A|i \rangle^2 N}{\sigma^2 + J^2}, \quad (45)$$

where we used the weak value formula (34). Consequently, as before we find the Fisher information is modified by a factor of order 1 (which will decrease or keep the Fisher information the same, as discussed before). This is the same conclusion reached by Knee and Gauger [32] and Ferrie and Combes [33], that the weak value amplification offers no increase of Fisher information for technical noise. This result was previously found by Feizpour, Xingxing, and Steinberg [34], who noted that this type 1 technical noise could not be suppressed by the real weak values technique. However, as we will show in Sec. II G, this is not the case for techniques implementing an imaginary weak value.

We go on to find the efficient estimator in the post-selected case, following the maximum likelihood method presented in Eq. (32,33). The efficient estimator is given by $\hat{d}_{KG} = (1/A_w N') \sum_{j=1}^{N'} (x'_j + \xi_j)$. In other words, one can efficiently estimate the parameter from the SNR. We note that in either the standard or WVA scheme, the Fisher information can be further improved by reducing the width of the meter state, but only until $\sigma \sim J$, after which the technical noise dominates the variance. We will return to this point in Sec. II G.

E. Type 2 technical noise: Correlated noise model of Feizpour, Xingxing, and Steinberg

In order to achieve the CRB, the Fisher information must not only be calculated, but the associated estimator must also be practical to implement. The point of practicality of the efficient estimator can be strongly made by considering the analysis of Feizpour, Xingxing, and Steinberg [34]. Consider an experiment with single photons, such that the measurement is only triggered by the photon detection at the detector, and consists of N measured variables

ϕ_j described by an average $\bar{\phi}$ plus a noise term η_j that is correlated in general, $\langle \eta_i \eta_j \rangle = C_{ij}$ (we define this as *type 2* technical noise). The noise term contains both quantum and technical noise. It is then straightforward to check that the average is given by $(1/N) \sum_{i=1}^N \phi_i = \bar{\phi}$, and the variance is given by $V = (1/N^2) \sum_{ij} \langle \phi_i \phi_j \rangle$. The two limits considered in Ref. [34] are (i) the white noise limit, $C_{ij} = C \delta_{ij}$, and (ii) the fully correlated limit $C_{ij} = C$. In case (i) we have $V = C/N$, while in case (ii), we have $V = C$. Thus averaging helps the SNR for white noise, but not for fully correlated noise.

Now consider the postselected case, where $\bar{\phi} \rightarrow \bar{\phi} A_w$, and $N \rightarrow N' = \gamma N$. In case (i), the variance is now C/N' , while the signal is $A_w \bar{\phi}$, so the SNR scales like $A_w \sqrt{\gamma}$, so the small post-selection probability drops out, indicating there is no advantage to using post-selection in this case (exactly as we calculated in the previous subsections for type 1 technical noise). However, in case (ii), the signal is boosted the same amount, while the variance remains C in the fully correlated case. Consequently, the SNR shows an advantage over the non-postselected case. Feizpour, Xingxing, and Steinberg go on to consider a particular noise model consisting of a combination of white and time-correlated noise, showing this advantage remains so long as the correlation time remains long compared to the photon production rate (as it is in many optical implementations).

We can now revisit this model in the context of the Fisher information metric to see how it compares to the SNR metric. The joint probability distribution of all of the variables ϕ_i can be written, assuming Gaussian statistics, as

$$P_S(\mathbf{x}) = \frac{1}{\sqrt{(2\pi)^N \det \mathbf{C}}} \exp \left[-\frac{(\mathbf{x} - \boldsymbol{\mu})^T \cdot \mathbf{C}^{-1} \cdot (\mathbf{x} - \boldsymbol{\mu})}{2} \right]. \quad (46)$$

Here, \mathbf{x} is a vector of elements ϕ_i , and $\boldsymbol{\mu}$ is a vector of the means (in this case, $\boldsymbol{\mu} = \bar{\phi} \mathbf{1}$ is a vector with the same mean in every element). The matrix \mathbf{C} is the covariance matrix and has elements C_{ij} . \mathbf{C}^{-1} is the inverse of the covariance matrix, and $\det \mathbf{C}$ is its determinant.

In this case, we may calculate the Fisher information (29) about $\bar{\phi}$ contained in this distribution, and obtain,

$$\mathcal{I}_S = \partial_{\bar{\phi}} \boldsymbol{\mu}^T \cdot \mathbf{C}^{-1} \cdot \partial_{\bar{\phi}} \boldsymbol{\mu} = \sum_{i,j=1}^N C_{ij}^{-1}. \quad (47)$$

Notice this Fisher information contains a double sum of the elements of the inverse covariance matrix. The “diagonal” terms describe the self-correlation terms, and scale proportionally to N , recovering the independent trials for the case when the covariance matrix is diagonal. However, for strong correlations, such as the type Feizpour, Xingxing, and Steinberg consider, each element of the inverse covariance matrix can be of comparable value, so the Fisher information can scale at most like N^2 , giving a much larger Fisher information than for uncorrelated noise. The reason is because of the correlations between the different measurements that the SNR metric misses.

When we go to the postselected case, the dimension of the matrix shrinks from N to γN , while the mean is boosted by $A_w \sim \gamma^{-1/2}$. The Fisher information is boosted by $1/\gamma$ as before, but the double sum in (47) now only goes to γN in the upper limit, $\mathcal{I}'_S = A_w^2 \sum_{i,j}^{\gamma N} C_{ij}'^{-1}$. The covariance matrix is different in general, since it now describes the correlations between the postselected photons only. Consequently, for white noise the Fisher information is the same, up to a factor of order 1, while for highly correlated noise, the Fisher information scales at most as $N^2 \gamma$, so it is actually decreased by a factor of γ by the weak value technique, compared to the non-postselected case. It is easy to see why: the correlations of any single postselected photon with any rejected photon are lost in the detection scheme (unless further processing of the correlated missing photons is done), and consequently cannot be harnessed to further suppress the noise. In contrast to this, if the photon is correlated only with itself, then taking a random postselection will not hurt, and the Fisher information can stay the same.

However, this is not the whole story. We must ask what estimator should be used that saturates the CRB, and whether it is practical to implement it. We can find this estimator using maximum likelihood methods described earlier (32,33) to find the estimator $\hat{\phi}$. We assume that the covariance matrix is positive definite, symmetric, and invertible. It then follows that its inverse is also symmetric. We find the estimator in the non post-selected case to be

$$\hat{\phi}_S = \frac{\sum_{i,j=1}^N C_{ij}^{-1} \phi_j}{\sum_{i',j'=1}^N C_{i'j'}^{-1}}. \quad (48)$$

We can check the variance of this estimator matches the CRB,

$$\langle (\hat{\phi}_S - \bar{\phi})^2 \rangle = \frac{\sum_{i,j,k,l} C_{ij}^{-1} C_{kl}^{-1} \langle (\phi_j - \bar{\phi})(\phi_l - \bar{\phi}) \rangle}{\left(\sum_{i',j'} C_{i'j'}^{-1} \right)^2}, \quad (49)$$

because the correlation of the two random variables gives the elements of the covariance matrix, C_{jl} , which cancels one of the inverse matrices in the sums, giving one factor of the denominator, resulting in the CRB we found above, the inverse of (47).

However there is a difficulty in this result: The experiment implementing the estimator (48) must multiply every data point ϕ_j by a different weighting factor, $f_j = \sum_{i=1}^N C_{ij}^{-1} / \sum_{i',j'=1}^N C_{i'j'}^{-1}$, which knows about the rest of the data points. The experimenter must know exactly what the correlations are, how many data points are being collected, and must be able to weight each data point by a different factor in order to extract the maximal information in the data average. This is generally a very challenging experimental task. Therefore, the SNR, which treats every type of noise on equal footing (so the weighting assignment is $f_j = 1/N$ for all j) is usually the most practical option. Consequently, the SNR, although suboptimal as a means for estimating in this case, is still superior since the optimal estimator is impractical to implement for typical experiments. This is why the SNR is used by experimentalists: because a complete categorization of the noise correlations is a formidable task requiring detailed knowledge of noise correlations and extensive post-processing. If we go on to consider non-Gaussian correlated noise, such as $1/f$ noise, the problem of implementing the estimator becomes even worse.

F. Type 3 technical noise - air turbulence

Another type of technical noise that is very important in open air experiments is turbulence, which we refer to here as type 3 technical noise. While we will not give a quantitative analysis of this effect here, it gives additional beam width broadening beyond the diffraction limit because of beam breathing (on a short time scale), and beam wander (on a longer time scale) because of the propagation through the random medium [39]. This becomes an important problem when there is a large optical path length from the position where the deflection occurs to the detector where it is measured. Beam jitter from turbulence cannot be underestimated when dealing with extremely small deflections. The beam wander effects become important on time scales longer than the ratio of the beam width to the typical air velocity. Typical experiments can run between seconds and hours, so this effect must be accounted for. The weak values schemes have a distinct advantage over the standard beam deflection measurement in having short optical path lengths. We will see this in detail in the next subsection.

G. Imaginary weak values and technical advantages

We proceed to consider situations where imaginary WVA has technical advantages for combined technical noise types. Kedom points out that in the case of imaginary weak values, noise in the average position does not appear in making measurements in the momentum basis, and that noise on the average momentum helps the SNR [35]. We focus on a different effect unique to imaginary weak values. For definiteness, consider beam deflection measurements for a coherent Gaussian beam using standard deflection techniques versus a Sagnac interferometer weak value experiment. Most experiments used to date that show technical advantages use imaginary weak values.

To start, assume that the system has no technical noise. The unknown parameter of interest is the deflection k of the beam, which can be interpreted as the transverse momentum kick given by a mirror. Treps *et al.* showed that one can interfere a local oscillator of a first order TEM mode to achieve the optimal Fisher information [22]. However, for simplicity and to understand the role of beam diameters we consider a more standard approach. A tilt or deflection on a beam requires propagation to observe a displacement. The standard method of measuring an unknown mirror tilt k with a beam of width σ is to propagate the light and focus it with a lens, thereby taking the Fourier transform of the beam by measuring the beam with a split detector in the back focal plane of the lens (see Fig.11(a) assuming $q = 0$). The lens transforms the tilt k into a displacement fk/k_0 on the detector, where f is the focal length and k_0 is the wavenumber. The lens takes the beam width σ at the mirror to a beam width at the focus given by $\sigma_f = f/2k_0\sigma$.

The single photon probability distribution function is then

$$p_H(x|k) = \mathcal{N} \exp \left[-\frac{(x - fk/k_0)^2}{2\sigma_f^2} \right], \quad (50)$$

where \mathcal{N} is a normalization. If we send N independent photons to measure k , this yields a Fisher information of

$$\mathcal{I}_H = \frac{N(f/k_0)^2}{\sigma_f^2} = 4N\sigma^2, \quad (51)$$

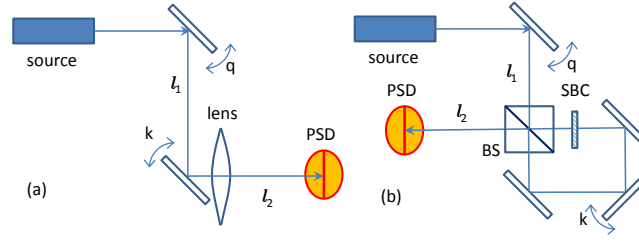


FIG. 11. Two strategies to detect an unknown constant momentum kick k given angular jitter of momentum q . (a) Standard method: After the momentum kick, the beam propagates a distance l_1 before getting a momentum kick k from the mirror, that is the parameter we wish to estimate. The beam then passes through a lens with a focus $f = l_2$, chosen to equal the distance traveled until it comes to the split detector, where the beam reaches its focus as a position sensitive detector (PSD). (b) Weak value type method: After the momentum jitter kick q , the light enters a Sagnac interferometer, comprised of a 50/50 beam splitter (BS), Soleil-Babinet compensator (SBC), which introduce a relative phase shift ϕ between the paths, other mirrors, including the one that has the the momentum kick k we wish to measure. The beam ends at a position sensitive detector (PSD)

which is an intuitive result. This means that in order to get the smallest beam waist in the back focal plane, one wants the largest beam waist possible before the lens. We now compare this with the Sagnac interferometer weak values result.

The weak value technique for measuring the beam deflection (Fig. 11(b) with $q = 0$) gives the post-selected distribution, that when properly normalized, is a Gaussian distribution with mean $4k\sigma^2/\phi$ and width σ^2 . Here, ϕ is the phase difference of clockwise and counter-clockwise photons in the interferometer applied by the Soleil-Babinet compensator (SBC). This applies only to the post-selected fraction $N' = \gamma N$ of the photons that satisfy the postselection criterion, where $\gamma = \phi^2/4$. The postselected single photon probability distribution function is then

$$p'_H(x|k) = N' \exp \left[-\frac{(x - 4k\sigma^2/\phi)^2}{2\sigma^2} \right]. \quad (52)$$

The Fisher information for the postselected measurements, reduced by the postselection probability γ ($N \rightarrow \gamma N$) is then found to be

$$\mathcal{I}'_H = (\gamma N) 4\sigma^4 / (\gamma \sigma^2) = 4\sigma^2 N. \quad (53)$$

Thus, the weak values and standard method result in *the same* amount of classical Fisher information, as shown in Sec. II C, see also [40]. It is important to realize that this calculation is only valid in the regime of small angles $\sin^2(\phi/2) \approx \phi^2/4$. In other words, in the small angle or weak value regime, all of the Fisher information is in the photons leaving the dark port of the interferometer.

So how does noise affect the Fisher information for the two methods? As a first step, we will assume that there is no transverse beam deflection jitter, but only transverse detector jitter. In other words, there is a small transverse deflection k with no technical noise on the beam, but the detector used to measure the beam has a transverse jitter ξ that we only sample at the photon arrival times, giving type 1 technical noise. We first consider the standard method. As before, the new likelihood function is the convolution of the technical noise-free likelihood function with a Gaussian of width J . This simply increases the average beam waist at the detector by $\sqrt{\sigma_f^2 + J^2}$, resulting in a Fisher information

$$\mathcal{I}_N = \frac{N(f/k_0)^2}{\sigma_f^2 + J^2} = \frac{4N\sigma^2}{1 + \left(\frac{2k_0\sigma J}{f}\right)^2}. \quad (54)$$

This is a rather interesting result. It means that this approach can achieve the maximum Fisher information (as if there were no noise at all), but only in the limit of large focal length ($f \gg 2k_0\sigma J$). A large focal length is equivalent to opting for a larger displacement ($f k/k_0$) while allowing for a large focal spot ($\sigma_f \gg J$). This is once again an intuitive result: If a very small focal spot lands on a detector that has Gaussian random shifts, large differential intensity fluctuations will occur, due to detector jitter, compared with a large focal spot.

For the imaginary weak value approach, the results are quite different. The beam waist for this case is given by σ , not the focused beam waist σ_f . This gives a Fisher information of

$$\mathcal{I}'_N = \frac{4N\sigma^4}{\sigma^2 + J^2}. \quad (55)$$

Therefore, since $\sigma \gg \sigma_f$ and there is freedom to choose σ as large as one wishes, we can make the beam waist much larger than J , which both suppresses J and increases the Fisher information (53). This shows that Fisher information for the imaginary weak values approach remains unchanged in the presence of transverse detector jitter, while the focused beam approach requires long focal lengths.

Hence, the measurement geometry plays a very important role in several ways. Ideally one would like a detector with a continuous detection distribution, but practical considerations mean there will always be dead space between finite width detectors. A simple method for obtaining nearly optimal beam detection is split detection. However, even in this case there is always a gap between the detectors, which sets a minimum beam diameter and thus a finite propagation through horizontal turbulence. This is not a problem for weak values since the detector can be placed immediately after the last beam splitter which mitigates the type 3 technical noise while also suppressing type 1 technical noise. The standard method operating in the regime where type 1 noise is completely ameliorated will suffer from the type 3 technical noise.

H. Type 4 technical noise - angular beam jitter

We now consider angular beam jitter by modeling it as a random momentum kick q given to the beam before it enters the interferometer, or before it approaches the signal mirror in the standard method. This kick could be from air turbulence or mirror jitter.

1. Standard method results for angular jitter

We first consider the standard method of measuring the beam displacement illustrated in Fig. 11(a). The Fourier optics of this geometry is described by a series of unitary operators that act on the transverse degree of freedom in the paraxial approximation. Starting from an initial transverse state $|\psi\rangle$, that we take to be a Gaussian in transverse position with zero mean, and variance σ^2 , the unitary $U_q = \exp(iq\hat{x})$ gives the first random momentum kick q to the beam. This is followed by a propagation of distance l_1 , given by the unitary $U_{l_1} = \exp(-i\hat{p}^2 l_1 / 2k_0)$, where k_0 is the wavenumber of the light. This is followed by a momentum kick k described by $U_{q \rightarrow k}$, and then the lens which gives a quadratic phase front, $U_f = \exp(-ik_0 \hat{x}^2 / 2f)$. The final propagation U_{l_2} puts the beam at the measurement device, which is a position-sensitive detector (PSD).

Taken together, we can describe the final state as

$$\psi_d(x) = \langle x | U_{l_2} U_f U_k U_{l_1} U_q | \psi \rangle. \quad (56)$$

To obtain an explicit form for the state, and the expectation of the position and its variance in this state, a series of complete sets of states are inserted between the unitaries. As an intermediate step, let us define state ψ_i as the state after the k momentum kick, but before the lens. The action of the lens is diagonal in the position basis, but the subsequent propagation is diagonal in the momentum basis. Defining the coordinate at the detector as x , the state at the detector $\psi_d(x)$ is given by

$$\psi_d(x) = \int \frac{dp}{2\pi} \int dy \psi_i(y) e^{-ik_0 y^2 / 2f - ipy} e^{-ip^2 l_2 / 2k_0 + ipx}. \quad (57)$$

We can reverse the order of integration and perform the p integration first. This gives

$$\psi_d(x) = \sqrt{\frac{k_0}{2\pi i l_2}} \int dy \psi_i(y) e^{-ik_0 y^2 / 2f + i(y-x)^2 k_0 / 2l_2}. \quad (58)$$

Let us choose $l_2 = f$, so the quadratic terms in the exponential cancel out, which will lead to focusing the beam. This leaves the state as

$$\psi_d(x) = \sqrt{\frac{k_0}{2\pi i l_2}} e^{ik_0 x^2 / 2f} \int dy \psi_i(y) e^{-iyk_0 x / f}, \quad (59)$$

which simply gives the scaled Fourier transform of ψ_i , but with a particular value of the momentum, $\tilde{\psi}_i(p \rightarrow k_0 x / f)$.

The remainder of the solution involves finding the intermediate state. This is straightforward in the momentum basis, because the first three operators are diagonal in this basis. Therefore, the momentum-space expression for ψ_i is given by

$$\tilde{\psi}_i(p) = (8\pi\sigma^2)^{1/4} \exp(-\sigma^2(p + q + k)^2 - il_1(p + k)^2 / 2k_0). \quad (60)$$

Putting these results together, we find that the final state at the detector gives a Gaussian distribution in position x with average and variance of

$$\langle x \rangle = -(k+q)f/k_0, \quad \langle (x - \langle x \rangle)^2 \rangle = f^2/(2\sigma k_0)^2. \quad (61)$$

The net result is that the random momentum kick q simply adds to the signal k . Averaging this distribution of Gaussian random jitter of momentum q with zero mean and variance Q^2 gives another Gaussian distribution for x , of mean $-kf/k_0$ and wider variance $f^2[1/(2\sigma k_0)^2 + Q^2/k_0^2]$. Thus, the Fisher information, for N independent measurements, about k in this distribution is given by

$$\mathcal{I}_d = \frac{4N\sigma^2}{1 + (2\sigma Q)^2}. \quad (62)$$

2. Weak value treatment of angular jitter

A similar analysis can be carried out for the weak value interferometer case. In addition to the momentum kick and the propagation steps, there are two unitaries that depend on the which-way operator $\hat{W} = |\circ\rangle\langle\circ| - |\odot\rangle\langle\odot|$, where the states $|\circ\rangle, |\odot\rangle$ are clockwise and counterclockwise moving photon states inside the Sagnac interferometer. Superpositions of these states are created by the 50-50 beam splitter operating on the incoming beam. The unitaries are the relative phase shift operator, $U_\phi = \exp(i\phi\hat{W}/2)$, induced by the SBC, and the which-path momentum kick operator, $U_{Wk} = \exp(ik\hat{W}\hat{x})$ delivered by the signal mirror.

As shown in Fig. 11(b), starting in the state $|\Psi_i\rangle = |\psi\rangle(|\circ\rangle + i|\odot\rangle)/\sqrt{2}$, and ending in state $|\Psi_f\rangle = |x\rangle(|\circ\rangle - i|\odot\rangle)/\sqrt{2}$, we seek the transition amplitude

$$\langle \Psi_f | U_{l_2} U_{kW} U_\phi U_{l_1} U_q | \Psi_i \rangle, \quad (63)$$

which describes photons entering in one interferometer port and exiting the other interferometer port. Fortunately, the which-path states pass through all but two of the operators, so this amplitude may be simplified to eliminate the which-path states and operators, giving the state of the transverse beam at the detector, $\psi_{wv}(x)$, to be

$$\psi_{wv}(x) = \langle x | e^{-i\hat{p}^2 l_2/2k_0} \sin(k\hat{x} + \phi/2) e^{-i\hat{p}^2 l_1/2k_0} e^{iq\hat{x}} | \psi \rangle. \quad (64)$$

The detailed calculation of this state involves inserting complete sets of states, resulting in a complicated expression. The result is simplified by expanding to linear order in ϕ and k since we assume the weak value ordering of parameters, $k\sigma < \phi < 1$. We must renormalize the post-selected distribution by the probability γ of a photon exiting the dark port, given by

$$\gamma = (\phi/2)^2 + k^2\sigma^2 + \mathcal{O}(k^2q^2) + \mathcal{O}(\phi kq) + \dots \quad (65)$$

We drop the other terms compared with $(\phi/2)^2$, so the phase shift ϕ controls the post-selection. This gives an average displacement of

$$\langle x \rangle = \frac{4k\sigma^2}{\phi} + \frac{kl_1(l_1 + l_2)}{k_0^2\phi\sigma^2} + \frac{q(l_1 + l_2)}{k_0} + \dots \quad (66)$$

where we suppress higher order terms in k, q, ϕ . The first term of order k is the usual weak value term, amplified by $1/\phi$ [5]. The second term comes from the diffraction effects which gives a small correction to the first term because we take $\sigma^2 \gg \sqrt{l_1(l_1 + l_2)}/2k_0$. The remaining term, $q(l_1 + l_2)/k_0$ is just the free propagation from the momentum kick, and has a geometric optics interpretation of the imparted deflection angle q/k_0 times the total length of propagation. We note that the way q enters into the average displacement has a very different form than Eq. (61). We will return to this shortly. The displacement variance at the detector may be similarly calculated to find,

$$\langle (x - \langle x \rangle)^2 \rangle = \sigma^2 + \left(\frac{l_1 + l_2}{2k_0\sigma} \right)^2, \quad (67)$$

plus further corrections of order k^2 . Thus, we see that the diffraction effects broaden the width of the beam, proportional to the total path length. If we approximate the distribution as a Gaussian with the mean and variance discussed above, the Fisher information about k can be found by averaging over q as before to find

$$\mathcal{I}_{wv} = \frac{4N\sigma^2}{1 + \left(\frac{l_1 + l_2}{2k_0\sigma^2} \right)^2 (1 + (2\sigma Q)^2)}. \quad (68)$$

Consequently, even if σQ is large compared to 1, so as to degrade the Fisher information in the standard method (62), in the weak values technique, there is an additional suppression factor of the amount of diffraction, $(l_1 + l_2)/(2k_0\sigma^2) \ll 1$, indicating that the weak value technique outperforms the standard method when dealing with angular jitter. This result can be understood intuitively because the angular jitter directly adds to the detected deflection in the standard measurement case, whereas it is only a small correction to the deflection that is controlled by diffraction in the weak value technique.

The rather remarkable properties associated with imaginary weak value experiments may not be entirely attributed to weak values, but to geometric terms associated with the experiments. These terms, such as beam waist diameter, arise even when WVA is small. However, it is important to note only in the limit of large WVA that all of the information in the measurement can be placed in the measured photons and that optimal SNR estimation of the parameter can be made. Therefore, these geometric terms and WVA work hand-in-hand to achieve the technical noise suppression.

I. Fisher Information for recycled photons

We can also consider the possible benefit to the Fisher information of the photon recycling proposal discussed in the previous section [19]. Considering photons as a resource, one can ask what the maximum amount of information can be extracted from a given set of photons. In much the same way as a high finesse cavity can increase phase sensitivity in an interferometer, recycling photons from the bright port of a weak value experiment can increase the information about a parameter. As discussed previously, the goal is to postselect all of the photons while keeping the large weak value amplification. The scheme is to recycle the rejected photons by closing off the interferometer, so the remaining $N_1 = N - N'$ photons are re-injected ($N' = \gamma N$) and once again sample the unknown parameter k . We have discussed that it is important that the rejected light be reshaped to once again be in its original profile, otherwise all amplification of the split detector SNR is erased over many cycles. Below, we consider the simplest version where no propagation effects are included. In that case, the second round of postselected light has exactly the same distribution on the detector, with the same post-selection probability γ , so the Fisher information for this cycle is $\mathcal{I}_1 = (\gamma N_1)4\sigma^4/(\gamma\sigma^2) = 4\sigma^2 N_1$. This process is now repeated many times, where N_i is the number of rejected photons on the i^{th} round, and we define $N_0 = N$. The uniform postselection probability indicates that $N_i = N_{i-1}(1 - \gamma)$, implying that $N_i = N(1 - \gamma)^i$.

Since each measurement is independent from the last, the Fisher information simply adds, giving a total of

$$\mathcal{I}_{\text{tot}} = 4\sigma^2 \sum_{i=0}^{\infty} N_i = 4\sigma^2 N \sum_{i=0}^{\infty} (1 - \gamma)^i = \frac{4\sigma^2 N}{\gamma}. \quad (69)$$

Therefore, the Fisher information has been boosted by a factor of $1/\gamma$ compared to the standard method, or the single pass weak value method. Here, we are considering the photon number N as the resource. Of course, as is pointed out in the first section, one could have been sending more light onto the detector using the standard method in the time taken for the light recycling or employed other standard schemes, but there could be many technical reasons why this may be impossible or inadvisable given a laboratory set-up. There may be a minimum quiet time between laser pulses, for example, or the detector may have a low light power threshold. We note that the profile reshaping process actually removes information about the parameter k , but does so in a way that the estimator can be simply and easily implemented as the split detection SNR. Together with the technical advantages already discussed, this is an important improvement over previous techniques. A further possibility is to combine this technique with quantum light techniques, which would give a powerful advantage for estimating a parameter. The fact that all photons are now collected permits one to further mine interphoton correlations for noise suppression.

J. Section conclusions

We have shown how weak value based measurement techniques can give certain technical advantages to precision metrology. First and foremost, the Fisher information in a weak value measurement (which uses a small fraction of the available light) can be as large as the Fisher information of a standard measurement (which uses all of the available light). This is remarkable because the remaining light can be sent to another experiment [11], or recycled [19] to give even higher amounts of Fisher information.

We have also explored technical advantages the weak value experiments can have over standard measurement techniques. Obvious advantages, such as when the detectors saturate at a certain light intensity, have been pointed out in previous works [5, 9]. The possible advantages for different types of technical noise should be investigated on

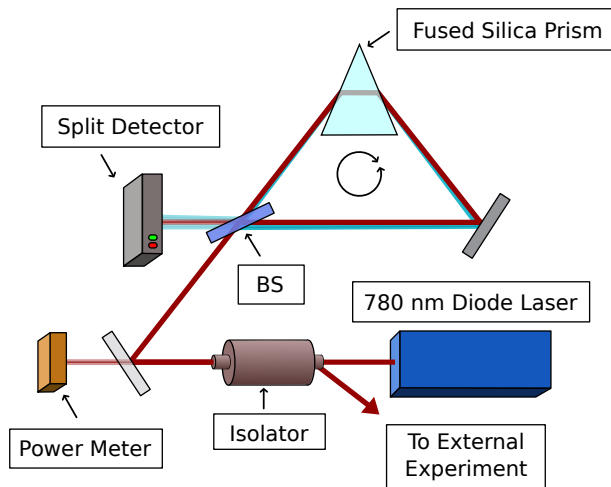


FIG. 12. A Gaussian laser beam passes through a Sagnac interferometer consisting of a 50:50 beam splitter (BS), a mirror and a prism. The prism weakly perturbs the direction of the beam as the frequency of the laser source is modulated, denoted by the red and blue beam paths. We monitor the position of the light entering the dark port of the interferometer. We lock the input power to the interferometer using a power measurement before the BS. The majority of the light exits the interferometer via the bright port and is collected with an isolator for use in an experiment.

a case by case basis. There are cases where the weak value techniques gives advantages, and other cases where it is at a disadvantage, and yet other cases where there is no difference. It is clear, for example, that dephasing noise will reduce the size of the weak value, which will be detrimental to this technique [41]. We have shown how detector noise, together with air turbulence can both be eliminated by a weak value deflection measurement, whereas the conventional standard method must suffer from turbulence jitter if detector noise is suppressed in open air experiments. We also demonstrated that for angular jitter, the weak value technique for beam deflection measurements can have much higher Fisher information than the standard technique. Considering the wide range of experiments that have now successfully employed weak value techniques to make high precision measurements [4–11, 15, 16, 34, 42], this should not be too surprising.

Another conclusion we reach is that it is not sufficient to show an estimator does not reach the CRB to decide it should be rejected. Rather, the optimal estimator should be found, and must be practically implementable. If it is not, the inefficient - but practical - estimator is superior. We have argued that time-correlated technical noise is one example where the difficulty of implementing the optimal estimator is outweighed by the option of implementing the postselection with amplification.

III. WEAK VALUE ENHANCED PRECISION FREQUENCY MEASUREMENTS

In the previous section, we discussed several different types of noise suppression that the weak value amplification technique can benefit from. Here, we show practical results of the weak value amplification technique for the purpose of precision frequency measurements [11].

Precision frequency measurements [43–45] of a stabilized laser source are of great importance in the field of metrology [46] as well as atomic, molecular [47] and optical physics [48]. We now report on our results, showing that weak values [1, 49] in an optical deflection measurement experiment [5] can produce frequency shift resolutions down to 129 ± 7 kHz/ $\sqrt{\text{Hz}}$ with only 2 mW of continuous wave optical power. By performing a weak measurement of the deflection of an infrared laser source that has passed through a weakly dispersive prism, we are able to measure a change in optical frequency comparable to precision Fabry-Perot interferometers [50–52]. This technique is relatively simple, requiring only a few common optical components and operating at atmospheric pressure. Additionally, we show that this technique has low noise over a large range of response frequencies, making it desirable for many applications such as Doppler anemometry [53], tests of the isotropy of light propagation [48] or laser locking without the use of high finesse Fabry-Perot interferometers [54] or atomic lines.

Theory.—We describe here the frequency amplification experiment shown in Fig. 12 by further developing the ideas we previously published in Ref. 5. Although the actual experiment uses a classical beam, we choose to characterize the weak value effect one photon at a time; this is valid, owing to the fact that we consider here a linear system with

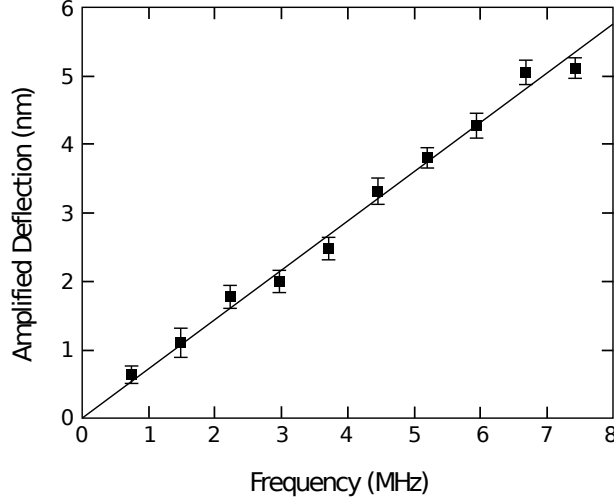


FIG. 13. The position of the postselected beam profile is measured as we modulate the input laser frequency of the interferometer. The modulation oscillates as a sine wave at 10 Hz and the signal from the split detector is frequency filtered and amplified. The error bars are given by the standard deviation of the mean. The minimum frequency change measured here is around 743 kHz with an effective integration time of 30 ms. The weak value amplification is approximately 79.

a coherent laser beam modeled as a linear superposition of Fock states [18].

In this experiment, a single-mode Gaussian beam of frequency ω and radius σ passes through an optical isolator, resulting in linearly polarized light. We assume that the radius is large enough to ignore divergence due to propagation. Light then enters a Sagnac interferometer containing a 50:50 beam splitter (BS), a mirror and a prism. The beam travels clockwise and counter-clockwise through the interferometer, denoted by the system states given by $\{|\odot\rangle, |\ominus\rangle\}$; we write the photon meter states in the position basis as $\{|x\rangle\}$, where x denotes the transverse, *horizontal* direction.

Initially, the interferometer (including the prism) is aligned such that the split photon wave function spatially overlaps (*i.e.*, the photons travel the same path whether by $|\odot\rangle$ or $|\ominus\rangle$). After the interferometer is aligned, the photons traversing each path receive a small, constant momentum kick in the *vertical* direction; this vertical kick is controlled by the interferometer mirror and results in a misalignment. Due to its spatial asymmetry about the input BS, this momentum kick creates an overall phase difference ϕ between the two paths. By adjusting the interferometer mirror, we can control the amount of light that exits the interferometer into the dark port. While the amplified signal ultimately depends on the value of the which-path phase shift, ϕ , and therefore on the magnitude of the misalignment, the SNR is unaffected (discussed below).

We then let $k(\omega)$ represent the small momentum kick given by the prism to the beam (after alignment) in the horizontal x -direction. The *system* and *meter* are entangled via an impulsive interaction Hamiltonian [5] (resulting in a new state $|\psi_i\rangle \rightarrow |\Psi\rangle$) such that a measurement of the horizontal position of the photon after it exits the interferometer gives us some information about which path the photon took.

We consider a horizontal deflection that is significantly smaller than the spread of the wave packet σ we are trying to measure, *i.e.*, $k(\omega)\sigma \ll 1$. In this approximation, we find that the postselected state of the photons exiting the dark port is given by

$$\langle\psi_f|\Psi\rangle = \langle\psi_f|\psi_i\rangle \int dx \psi(x)|x\rangle \exp[-ixA_w k(\omega)], \quad (70)$$

where the weak value, defined above, is given by $A_w = -i \cot(\phi/2) \approx -2i/\phi$ for small ϕ .

There are two interesting features of Eq. (70). First, the probability of detecting a photon has been reduced to $P_{ps} = |\langle\psi_f|\psi_i\rangle|^2 = \sin^2(\phi/2)$, and yet the SNR of an ensemble of measurements is nearly quantum limited [9] despite not measuring the vast majority of the light. Second, the weak value (which can be arbitrarily large in theory) appears to amplify the momentum kick $k(\omega)$ given by the prism; the resulting average position is given by $\langle x \rangle_W = 2k(\omega)\sigma^2|A_w| \approx 4k(\omega)\sigma^2/\phi$, where the angular brackets denote an expectation value. We can compare this to the standard deflection caused by a prism measured at a distance l which is given by $\langle x \rangle \approx lk(\omega)/k_0$, where k_0 is the wavenumber of the light.

In order to predict the deflections $\langle x \rangle$ or $\langle x \rangle_W$, we must know the form of $k(\omega)$. For a prism oriented such that it imparts the minimum deviation on a beam, the total angular deviation is given by $\theta(\omega) = 2 \sin^{-1}[n(\omega) \sin(\gamma/2)] - \gamma$,

where $n(\omega)$ is the index of refraction of the material and γ is the angle at the apex of the prism [55]. However, we are only interested in the small, frequency-dependent angular deflection $\delta(\omega) = \Delta\theta = 2 \Delta n \{[\sin(\gamma/2)]^{-2} - [n(\omega)]^2\}^{-1/2}$, where Δn ($\Delta\theta$) is the index change in the prism (angular deflection of the beam) for a given frequency change of the laser. The small *momentum kick* is expressed as $k(\omega) = \delta(\omega)k_0$, where k_0 is the wavenumber of the incoming light. We can then write the amplified deflection as

$$\langle x \rangle_W \approx \frac{8k_0\sigma^2(\Delta n/\phi)}{\sqrt{[\sin(\gamma/2)]^{-2} - [n(\omega)]^2}}. \quad (71)$$

The frequency-dependent index $n(\omega)$ of fused silica, which was used in this experiment, can be modeled using the Sellmeier equation [56]. We can therefore calculate the expected $\langle x \rangle_W$ using Eq. (71). However, to compute the ultimate sensitivity of this weak value frequency measurement, we must include possible noise sources. If we consider only shot-noise from the laser, the SNR for small ϕ is approximated by

$$\mathcal{R} \approx \sqrt{\frac{8N}{\pi}} k_0 \sigma \delta(\omega), \quad (72)$$

as shown in Ref. 9, where N is the number of photons used in the interferometer. Note that N is not the number of photons striking the detector, which is given by NP_{ps} . By setting $\mathcal{R} = 1$ and using modest values for N , σ and ω , we find that frequency sensitivities well below 1 kHz are possible. However, other sources of noise, such as detector dark current, radiation pressure and environmental perturbations will reduce the sensitivity of the device.

Experiment.—In our experimental setup (shown in Fig. 12), we used a fiber-coupled 780 nm external cavity diode laser with a beam radius of $\sigma = 388 \mu\text{m}$. The frequency of the laser was modulated with a 10 Hz sine wave using piezo controlled grating feedback. The frequency control was calibrated using saturation absorption spectroscopy of the hyperfine excited states of the rubidium D2 line[57]: $F = 3 \rightarrow F' = \{2 - 4 \text{ crossover}, 3 - 4 \text{ crossover}, 4\}$ transitions of rubidium 85 and the $F = 2 \rightarrow F' = \{1 - 3 \text{ crossover}, 2 - 3 \text{ crossover}, 3\}$ transitions of rubidium 87. Linearly polarized light was divided before the interferometer using a 50:50 BS (although an imbalanced ratio here would be ideal for practical applications). The light in one port was measured with a photodiode and used to lock the power at 2 mW with an acousto-optic modulator before the fiber. The interferometer was approximately $l = 27$ cm in length; the mirror used to adjust ϕ was approximately 6 cm from the input BS (measured counter clockwise) and the prism, made of fused silica, was approximately 5 cm from the input BS (measured clockwise). Although the prism was not symmetrically placed in the interferometer as described in the theory above, the results are the same aside from a global offset in position which can be subtracted off during processing. The interferometer was first aligned to minimize light in the dark port and then, using the aforementioned mirror, misaligned to allow a small percentage of the light ($\sim 2\text{-}5\%$) into the dark port. The position of this light was measured using a split detector (New Focus model 2921). The signal was passed through two 6 dB/octave bandpass filters centered at 10 Hz and amplified by a factor of about 10^4 .

For Fig. 13, we measured the peak of the deflection in each 100 ms cycle, repeated 25 times; we computed the average and the standard deviation of this set as we varied the change in the optical frequency. We find that the amplified deflection is a linear function of oscillating optical frequency given by about 720 ± 11 pm/MHz. Compared to the unamplified deflection of about 9.1 pm/MHz given by the expression for $\langle x \rangle$, this gives an amplification factor of 79 ± 1.2 and a computed P_{ps} of 1.3%; this agrees with the measured P_{ps} of 2-5% if we include the extra light present in the signal due to phase front distortions from imperfect optics.

A characteristic noise scan was taken and plotted in Fig. 14 with and without frequency modulation. The signal was passed directly from the split detector into the oscilloscope before performing a fast Fourier transform. Data was taken with and without a 7.4 MHz optical frequency modulation to show the noise floor over a large bandwidth. The noise at higher frequencies was similarly flat. Second, to test the range over which this device could function, we optimized the interferometer at the low-frequency end of the laser's tuning range and obtained a SNR of approximately 19 with the 7.4 MHz optical frequency modulation. We then tuned to the high-frequency end of the laser's tuning range ($\Delta f \approx 141$ GHz), without adjusting or recalibrating the interferometer, and obtained a SNR of 10. In fact, this range can be much larger so long as the weak value condition $k(\omega)\sigma \ll 1$ is satisfied; for our beam radius and optical frequency, we could in principle measure over a range of 5 THz, or about 10 nm.

For our experimental parameters, we can measure below 1 MHz of frequency change with a SNR around 1, as shown in Fig. 13. It should be noted that, although the time between measurements is a full 100 ms, our filtering limits the laser noise to time scales of about 30 ms. For analysis, we take this as our integration time in estimating N for each measurement. The resulting sensitivity for our apparatus is 129 ± 7 kHz/ $\sqrt{\text{Hz}}$; *e.g.*, if we had integrated for 1 s instead of 30 ms, this device could measure a 129 kHz shift in frequency with a SNR of 1. The error in frequency comes from the calibration described above. Using Eq. (72), we find that the ideal ultimate sensitivity is approximately 67 kHz/ $\sqrt{\text{Hz}}$. This implies that this apparatus, operating at atmospheric pressure with modest frequency filtering, is

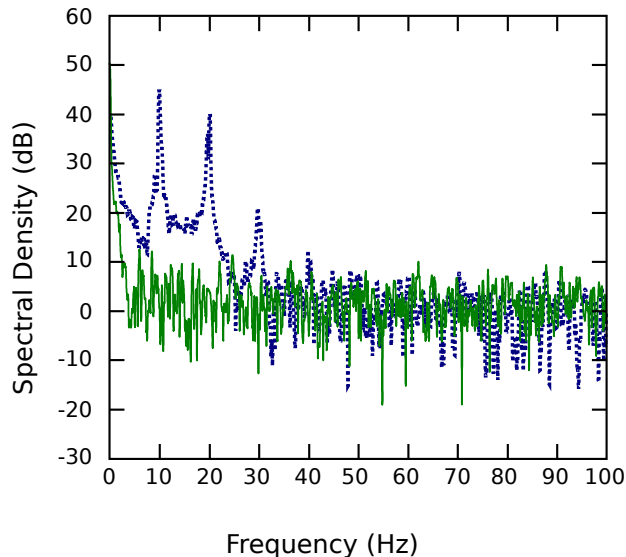


FIG. 14. We show the noise spectrum for a passive system (green, solid trace) and for a driven system (blue, dashed trace), where the laser frequency modulation is 7.4 MHz at 10 Hz. We see that the first harmonic of the signal is about 5 dB down from the fundamental and the third harmonic is nearly 25 dB down. For a 7.4 MHz change in laser frequency, we see that the noise is approximately 35 dB below the signal, demonstrating the low-noise nature of this measurement.

less than a factor of two away from the shot-noise limit in sensitivity. We discussed reasons for this close approach to the shot-noise limit in the previous section.

IV. PRECISION PHASE DIFFERENCE MEASUREMENTS

In the previous section, we discussed applications of weak value amplification to frequency difference measurements. In this section, we do the same, but for phase difference measurements, as reported on in Ref. [12]. The physics is somewhat different, because it reverses the size ordering of the parameters. Rather than have a small (known) phase shift amplifying a much smaller (unknown) momentum kick, it is the reverse. This leads to a qualitatively different different detector profile.

Phase measurements using coherent light sources continue to be of great interest in classical optics [58–62]. Not surprisingly, many advances in phase measurement techniques have been made since the introduction of the laser. For instance, Caves emphasized how the SNR of a phase measurement can be improved by using a squeezed vacuum state in the dark input port of an interferometer [20]. Related advances in this area include the use of other non-classical states of light such as Fock states [63] or the use of phase estimation techniques [64] which approach the Heisenberg limit in phase sensitivity [65]. Unfortunately, these states of light tend to be weak and very sensitive to losses, in effect reducing the SNR of a phase measurement. As a result, the use of coherent light sources has dominated the field of precision metrology [5, 66]. In this case, the phase sensitivity scales as $1/\sqrt{N}$ rad, where N is the average number of photons used in the measurement.

Perhaps the most famous contemporary phase measurement device is the laser interferometer gravitational-wave observatory (LIGO) [66, 67]. LIGO is a power-recycled Michelson interferometer with 4 km Fabry-Perot arms utilizing approximately ten Watts of input power. Although LIGO originally operated in a heterodyne arrangement using rf-sidebands, the second, “enhanced” stage will make use of a homodyne configuration [68]. The expected phase sensitivity of this device will be around 10^{-14} rad. However, the low saturation intensity of even state-of-the-art detectors limits the number of photons one can use in a given measurement with a fixed bandwidth.

We now show that it is possible to make a phase measurement with the same SNR as balanced homodyne detection yet only the light in the dark port is measured. We use a coherent light source with a split-detector in a Sagnac interferometer and show that the signal of a phase measurement is amplified. We derive our results using a classical wave description and summarize a quantum mechanical treatment which uses a similar weak value formalism to that presented in refs. [5, 9]. Much like with weak values [1], there is a large attenuation (post-selection) of the electric field (number of photons). Thus we can, in principle, use a low-cost detector with a low saturation intensity and still

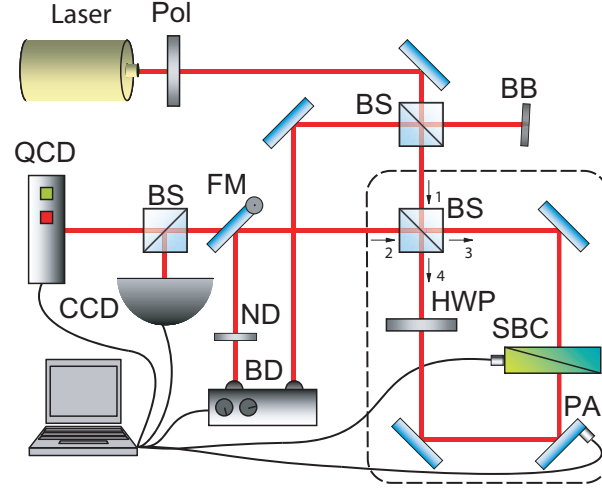


FIG. 15. (Color Online) Experimental setup. A coherent light source passes through a polarizer (Pol) producing horizontally polarized light before passing through the first 50/50 beamsplitter (BS). Half of the light strikes a beam block (BB) and is thrown out. The beam then enters the Sagnac interferometer via the second BS. One of the mirrors of the interferometer is controlled by a piezo actuator (PA) to precisely control the relative transverse momentum shift k . We use a half-wave plate (HWP) and a piezo-actuated Soleil-Babinet compensator (SBC) to produce a relative phase shift between the two light paths. During split-detection, we monitor the dark port using another BS that splits the light between a quad-cell detector (QCD) and a camera (CCD). During balanced homodyne detection, the interferometer is balanced and the flip-mirror (FM) is turned up, sending both bright and dark ports into the balance detector (BD). We use a neutral density filter (ND) in the bright port to correct for the light lost at the first BS.

obtain significantly higher phase sensitivity when compared to using a balanced homodyne detector with the same total incident intensity.

Theory — Consider a coherent light source with a Gaussian amplitude profile entering the input port of a Sagnac interferometer as shown in Fig. 15. The interferometer is purposely misaligned using a piezo-actuated mirror such that the two paths experience opposite deflections. The transverse momentum shift imparted by the mirror is labeled as k . A relative phase shift ϕ can be induced between the two light paths (clockwise and counterclockwise) in the interferometer.

We model the electric field propagation using standard matrix methods in the paraxial approximation. We can then write the input electric field amplitude as

$$\mathbf{E}_{in} = \begin{pmatrix} E_0 e^{-x^2/4\sigma^2} & 0 \end{pmatrix}^T, \quad (73)$$

where σ is defined as the Gaussian beam radius. The first position in the column vector denotes port 1 (see Fig. 15) of the beam splitter and the second position denotes port 2 (with no input electric field). We assume that the beam is large enough so that the entire Rayleigh range fits within the interferometer. The matrix representation for the 50/50 beamsplitter is given by

$$\mathbf{B} = \frac{1}{\sqrt{2}} \begin{pmatrix} 1 & i \\ i & 1 \end{pmatrix}, \quad (74)$$

where column and row one correspond to port 4 (counterclockwise) and column and row two correspond to port 3 (clockwise). We now define a matrix that gives both an opposite momentum shift k and a relative phase shift ϕ between the two light paths

$$\mathbf{M} = \begin{pmatrix} e^{i(-kx+\phi/2)} & 0 \\ 0 & e^{-i(-kx+\phi/2)} \end{pmatrix}. \quad (75)$$

The exiting electric field amplitude is represented by the matrix combination $(\mathbf{B}\mathbf{M}\mathbf{B})\mathbf{E}_{in}$,

$$\mathbf{E}_{out} = iE_0 e^{-x^2/4\sigma^2} \begin{pmatrix} -\sin(kx - \phi/2) \\ \cos(kx - \phi/2) \end{pmatrix}, \quad (76)$$

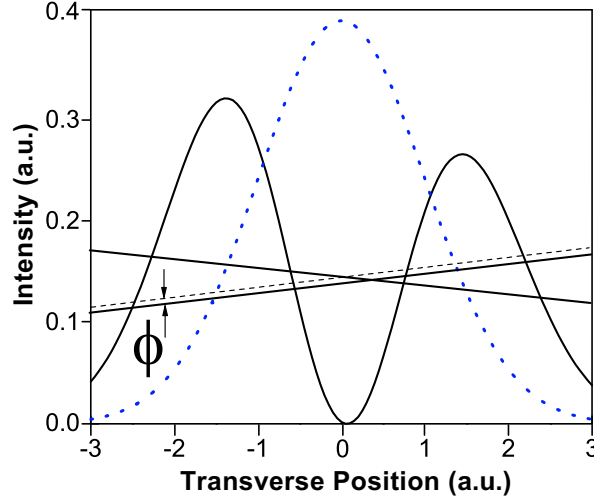


FIG. 16. (Color Online) Post-selected intensity distribution. The dotted (blue) curve is the single-mode input profile of the beam in the interferometer. The solid (black) curve is the post-selected split-Gaussian mode produced by the misalignment of the interferometer and a slight relative phase shift between the two light paths. The solid lines represent the tilted wave fronts in the two paths of the interferometer when they combine at the BS, one that is delayed relative to the other, producing an asymmetric split-Gaussian (shown). The dashed line represents a wave front with the same tilt but zero relative phase delay, which would result in a symmetric split-Gaussian (not shown).

where the first position now corresponds to port 2 (the dark port) and the second position corresponds to port 1 (the bright port).

For a balanced homodyne detection scheme, we take $k = 0$ and $\phi \rightarrow \pi/2 + \phi$ and subtract the integrated intensity of both ports. After normalizing by the total power, we obtain the unitless homodyne signal

$$\Delta_h = \sin(\phi). \quad (77)$$

Thus, we see that by balancing the interferometer, we are measuring the signal along the linear part of the sine curve for small phase shifts.

In contrast, if we consider a small transverse momentum shift ($k\sigma < 1$) and monitor only the dark port, given by the first element in the E_{out} vector, we find that

$$E_{out}^{(d)} \approx A \left(\frac{x}{\sigma} - \frac{\tan(\phi/2)}{k\sigma} \right) \exp[-x^2/4\sigma^2], \quad (78)$$

where $A = -iE_0k\sigma \cos(\phi/2)$. The intensity at the dark port is then given by

$$I_d(x) = P_{ps}I_0 \left(\frac{x}{\sigma} - \frac{\tan(\phi/2)}{k\sigma} \right)^2 \exp[-x^2/2\sigma^2], \quad (79)$$

where P_{ps} is the attenuation (post-selection probability) of the measured output beam given by

$$P_{ps} = |k\sigma \cos(\phi/2)|^2, \quad (80)$$

and I_0 is the maximum input intensity density. Aside from the attenuation factor P_{ps} , $I_d(x)$ is normalized for vanishingly small ϕ . Equation (79) is plotted in Fig. 16.

In order to have the greatest accessibility for our results, we have presented the theory here in terms of classical wave optics. However, for an analysis at the single photon level, and an analysis of the SNR for precision phase measurement, it is of interest to summarize the quantum mechanical derivation. The setup may be interpreted as the detection of the which-path (system) information of a single photon (clockwise or counter-clockwise). This is done indirectly using the transverse position degree of freedom of the photon as the meter, which is followed by a post-selection of the system state (due to the interference at the beam splitter), allowing only a few photons to arrive at the split-detector where the meter is measured.

If the pre- and post-selected system states are almost orthogonal (so $k\sigma \ll \phi \ll 1$), then there is an anomalously large shift of the beam's position, described by $A_w \approx -2i/\phi$ of the system (see Ref. [5]), as mentioned in the

previous section. The small overlap of the system's states gives rise to an amplification of the small momentum shift imparted by the mirror. However, in the present case, $\phi \ll k\sigma \ll 1$, so the situation does not have a straightforward interpretation in terms of weak values. Nevertheless, there are certain features in common: the amplification effect can be traced back to the fact that there is a renormalization of the state, owing to a small post-selection probability P_{ps} . A quantitative analysis shows that the meter deflection is now proportional to the *inverse weak value* A_w^{-1} ,

$$\langle x \rangle = -2 \operatorname{Im} A_w^{-1} \approx -\phi/k, \quad (81)$$

which may be interpreted as an amplification of the small phase shift by the mirror's momentum shift k . Notice that in contrast to the usual weak value case, the post-selected distribution is not a simple shift of the meter wavefunction, but in fact corresponds to a two-lobe structure [Eq. (79)] as seen in Fig. 16.

Instead of measuring the average position, one can use a split-detection method by integrating the intensity over the right side of the origin and subtracting from that the integrated intensity over the left side of the origin. This detection method is well suited to the split-Gaussian beam and results in a split-detection signal which, if normalized by the total power striking the detector, is proportional to the average position. This quantity is given by

$$\Delta_s \approx -\sqrt{\frac{2}{\pi}} \frac{\phi}{k\sigma} \approx \sqrt{\frac{2}{\pi\sigma^2}} \langle x \rangle. \quad (82)$$

Despite the large amplification of the average position measurement of the post-selected photons, the SNR is essentially the same for a balanced homodyne measurement of phase. The SNR of a phase measurement using balanced homodyne or split-detection can be expressed as $\mathcal{R}_{h,s} = \Delta_{h,s} \sqrt{N_d}$, where N_d is the number of photons striking the detector. These expressions are identical, except for an overall constant factor of $\sqrt{2/\pi}$. This reduces the SNR of the split-detection method by approximately 20%. It is also interesting to note that the SNR is independent of k . Thus, we can in principle reduce k (and P_{ps}) arbitrarily, allowing us to increase the input power and therefore N , ultimately improving the measurement sensitivity arbitrarily while using the same detector.

Experiment — In the present experiment (see Fig. 15), the coherent light beam was created using an external cavity diode laser tuned near the D_1 line of rubidium, approximately 795 nm. The beam was coupled into single mode fiber and then launched to produce a single mode Gaussian profile. The light was collimated with a radius of $\sigma \approx 775 \mu\text{m}$ and the continuous wave power ranged from 0.5 mW up to 1 mW. The Sagnac, composed of a 50/50 beam splitter and three mirrors, was rectangular. We used two configurations for the geometry of the interferometer, one with dimensions 39 cm x 8 cm (large) and another with dimensions 11 cm x 8 cm (small). The beam profile and position of the post-selected photons were measured using a quad-cell detector (QCD, New Focus model 2921) functioning as a split-detector and a CCD camera (Newport model LBP-2-USB). During balanced homodyne detection, the signal was measured using a Nirvana balance detector (BD, New Focus model 2007). The quantum efficiency of the BD was about 81%, whereas the quantum efficiency of the QCD was 75%. The QCD was also equipped with a protective glass plate with only 50% transmissivity. The outputs from the QCD and the BD were fed into two low-noise preamplifiers with frequency filters (Stanford Research Systems model SR560) in series.

We used a half-wave plate (HWP) with a piezo-actuated Soleil-Babinet Compensator (SBC) inside the Sagnac interferometer to induce a relative phase shift. The HWP was oriented such that the horizontally polarized input light was rotated to vertically polarized light. The SBC was oriented such that the fast axis was vertical and the slow axis was horizontal. The two light paths in the interferometer encountered these optical elements in opposite order, allowing for a known, tunable phase difference between them. The piezo-actuator in the SBC, which moved approximately 100 pm/mV, imparted a relative phase shift of $22 \pm 0.9 \mu\text{rad/V}$.

Using the large configuration, with 0.5 mW of input power, the piezo actuator in the SBC was driven with a 20 V peak to peak sine wave at 634 Hz, corresponding to a relative phase shift of 440 μrad . The normalized split-detection signal Δ_s (factoring in an offset from junk-light hitting the detector) was measured while the transverse momentum shift k was varied using the piezo-actuated mirror. After scaling Δ_s by the appropriate factor given in Eq. (82), the results were plotted in Fig. 17. The theory line, which corresponds to a relative phase shift of 440 μrad , is drawn along with the data. We see good agreement of the data with theory, with a clear inverse dependence of $\langle x \rangle$ on k . However, it should be noted that an determination of k for this fit requires calibration, which in practice is quite simple.

We then compared this split-detection method of phase measurement to a balanced homodyne measurement. We used the small configuration with 625 μW of (effective) continuous wave input power—taking into account various attenuators—and varied the driving voltage to the piezo-actuator in the SBC. The low-pass filter limits the laser noise to the 10% to 90% rise-time of a 1 kHz sine wave (300 μs). We take this limit as our integration time to determine the number of 795 nm photons used in each measurement. We measured the SNR of a phase measurement (see Fig. 18) using the same method as ref. [9] and found that the SNR of our homodyne measurement was on average 3.2 below an ideal quantum limited system. The SNR of our split-detection method was on average 2.6 times below an ideal

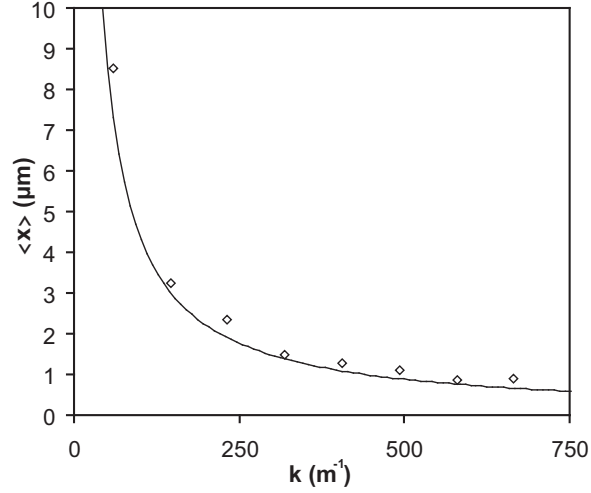


FIG. 17. Dependence on transverse momentum. The transverse momentum shift imparted by the piezo-actuated mirror was varied and the split-detection signal was measured using the QCD. The solid line is the theory curve from Eq. (81) using the expected phase shift.

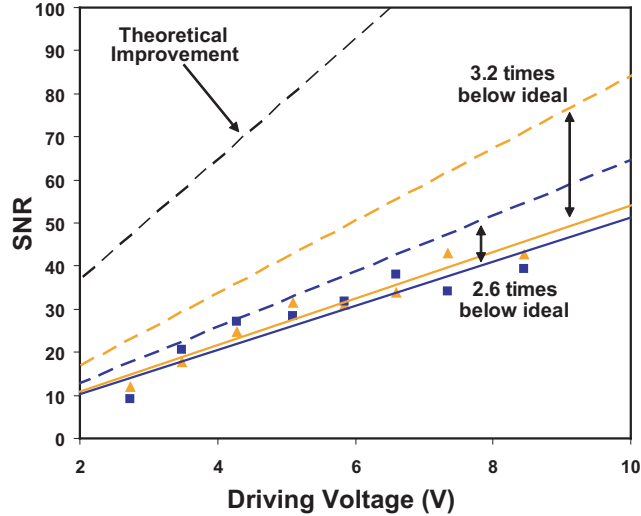


FIG. 18. (Color Online) Experimental comparison of split-detection to balanced homodyne. We vary the driving voltage applied to the piezo-actuator and measure the SNR using balanced homodyne detection (orange triangles) and the split-detection method (blue squares). The input power to the interferometer is approximately the same for both methods. Linear fits to the data (solid lines) show that these two methods have essentially the same sensitivity. The ideal quantum limited SNR (factoring in the quantum efficiency of each detector) is plotted using a dashed blue line (split-detection) or a dashed orange line (balanced homodyne detection). The dashed black line illustrates the theoretical (\sqrt{N}) improvement of the split-detection method assuming that an equal number of photons are incident on both the split-detector and the balance detector.

quantum limited system. We take into account the quantum efficiency of each detector for these two values, yet we ignore any contribution of dark current to the expected SNR.

Importantly, the SNR resulting from both measurement techniques is approximately the same. However, the split-detection method for this data had only about 15% of the input light incident on the detector. Thus, for diodes with the same saturation intensity, it is possible to use almost seven times more input power with this configuration, resulting in a SNR about 2.6 times higher (the black, dashed line in Fig. 18). The improvement of the SNR by taking advantage of the attenuation before the detector has no theoretical limit and is only limited in practice by phase front distortions and back-reflections off of optical surfaces which degrade the fidelity of the interference. Using commercially available equipment and one day of integration time, sub-picoradian sensitivity is possible even with a low-saturation intensity split-detector.

Part II

Further results concerning weak values and weak measurements

In the course of this investigation, we discovered and developed a number of theoretical results concerning generalized measurements and weak values that we will now summarize briefly so as to keep the report from getting too lengthy.

A. Contextual Values

There has been a conceptual gap between the notion of an observable operator on one hand, and the notion of how to measure such an observable when the measurement is not projective. We introduced contextual values [49] as a generalization of the eigenvalues of an observable that takes into account both the system observable and a general measurement procedure. This technique leads to a natural definition of a general conditioned average that converges uniquely to the quantum weak value in the minimal disturbance limit. This approach gives a theoretical grounding of the quantum weak value by providing a more general framework. We give several examples of how that framework relates to existing experimental and theoretical results. The theory of contextual values extends the well-established theory of generalized state measurements by bridging the gap between partial state collapse and the observables that represent physically relevant information about the system. We also wrote a lengthy extension of these theoretical results [69] to connect them more closely with both the quantum operations literature and other known results in pre and post-selected systems.

B. Two-Party Leggett-Garg Inequalities with Semiweak Measurements

In joint theory/experimental work of the Jordan and Howell group [70], we generalize the derivation of Leggett-Garg inequalities to systematically treat a larger class of experimental situations by allowing multi-particle correlations, invasive detection, and ambiguous detector results. Furthermore, we show how many such inequalities may be tested simultaneously with a single setup. As a proof of principle, we violate several such two-particle inequalities with data obtained from a polarization-entangled biphoton state and a semi-weak polarization measurement based on Fresnel reflection. We also point out a non-trivial connection between specific two-party Leggett-Garg inequality violations and convex sums of strange weak values (values outside of the eigenvalue range).

C. Measuring Which-Path Information with Coupled Electronic Mach-Zehnder Interferometers

We now summarize work done on electron Mach-Zehnder interferometers [71], and how one interferometer can be used as a detector for which-path information in a coupled interferometer. Once the detector is calibrated, we calculate weak values that arise when one detector current is conditioned on the outcome of the neighboring current. The use of contextual values mentioned above enables the precise construction of which-path operator averages that are valid for any measurement strength from the available drain currents. The form of the contextual values provides direct physical insight about the measurement being performed, providing information about the correlation strength between system and detector, the measurement inefficiency, and the proper background removal. We find that the detector interferometer must display maximal wave-like behavior to optimally measure the particle-like which-path information in the system interferometer, demonstrating wave-particle complementarity between the system and detector. We also find that the degree of quantum erasure that can be achieved by conditioning on a specific detector drain is directly related to the ambiguity of the measurement. Finally, conditioning the which-path averages on a particular system drain using the zero frequency cross-correlations produces conditioned averages that can become anomalously large due to quantum interference; the weak coupling limit of these conditioned averages can produce both weak values and detector-dependent semi-weak values. This system has recently been experimentally realized [72], and the experiment demonstrates the quantum eraser effect.

D. The significance of the imaginary part of the weak value

An important element of the weak value amplification experiments is the use of the imaginary weak value. However, a central question is whether or not this can be interpreted as a conditioned average of that observable in the limit of zero measurement disturbance. Unlike the real weak value, which can be understood as a conditioned average, we show [73] that the imaginary part of the generalized weak value does not provide information pertaining to the observable being measured. What it does provide is direct information about how the initial state would be unitarily disturbed by the observable operator. Specifically, we provide an operational interpretation for the imaginary part of the generalized weak value as the logarithmic directional derivative of the post-selection probability along the unitary flow generated by the action of the observable operator. To obtain this interpretation, we revisit the standard von Neumann measurement protocol for obtaining the real and imaginary parts of the weak value and solve it exactly for arbitrary initial states and post-selections using the quantum operations formalism, which allows us to understand in detail how each part of the generalized weak value arises in the linear response regime. We also provide exact treatments of qubit measurements and Gaussian detectors as illustrative special cases, and show that the measurement disturbance from a Gaussian detector is purely decohering in the Lindblad sense, which allows the shifts for a Gaussian detector to be completely understood for any coupling strength in terms of a single complex weak value that involves the decohered initial state.

E. Weak values are universal in von Neumann measurements

The theoretical phenomena of weak values only exists in the limit where the interaction strength goes to zero. However, all real experiments work at a finite interaction strength. It is therefore natural to ask if there is any general result that holds at finite measurement strength. We find that for the commonly used “von Neumann” interaction model, the answer is yes [74]. To do so, we refute the widely held belief that the quantum weak value necessarily pertains to weak measurements. To accomplish this, we use the transverse position of a free particle as the detector for the conditioned von Neumann measurement of a system observable. For any coupling strength, any initial states, and any choice of conditioning, the averages of the detector position and momentum are completely described by the real parts of three generalized weak values in the joint Hilbert space. Higher-order detector moments also have similar weak value expansions. Using the Wigner distribution of the initial detector state, we find compact expressions for these weak values within the reduced system Hilbert space. As an application of the approach, we show that for any Hermite-Gauss mode of a paraxial beam-like detector these expressions reduce to the real and imaginary parts of a single system weak value plus an additional weak-value-like contribution that only affects the momentum shift.

F. Quantum instruments as a foundation for both states and observables

This more theoretical approach works directly from the measured results to make predictions or retrodictions [75]. We demonstrate that quantum instruments can provide a unified operational foundation for quantum theory. Since these instruments directly correspond to laboratory devices, this foundation provides an alternate, more experimentally grounded, perspective from which to understand the elements of the traditional approach. We first show that in principle all measurable probabilities and correlations can be expressed entirely in terms of quantum instruments without the need for conventional quantum states or observables. We then show how these states and observables reappear as derived quantities by conditioning joint detection probabilities on the first or last measurement in a sequence as a preparation or a post-selection. Both predictive and retrodictive versions of states and observables appear in this manner, as well as more exotic bidirectional and interdictive states and observables that cannot be easily expressed using the traditional approach. We also revisit the conceptual meaning of the Heisenberg and Schrödinger pictures of time evolution as applied to the various derived quantities, illustrate how detector loss can be included naturally, and discuss how the instrumental approach fully generalizes the time-symmetric two-vector approach of Aharonov *et al.* to any realistic laboratory situation.

V. CONCLUSIONS

In this report we have described numerous projects worked on by the Jordan and Howell groups based on the theme of weak measurements, weak values and metrology in years 2010-2013.

We discussed a proposed weak value recycling scheme, where we have shown how a single optical pulse can be trapped inside the interferometer using a Pockels cell and the polarization of the pulse. Once trapped, all the photons

can eventually exit the dark port while retaining an amplified position, greatly boosting the sensitivity of the precision measurement. Pulse reshaping is important for the effect to not degrade over time. The added power accumulated at the detector within a fixed duration of time is the dominant source of sensitivity gain. Further increases are achievable by trapping multiple pulses in the interferometer simultaneously.

Next, we discussed the precise nature of the technical advantages of weak value amplification using the Fisher information measure in the presence of technical noise sources. We demonstrated that the weak value technique concentrates all the Fisher information about the parameter into just the post-selected fraction. When technical noise is added, there can be situations where the weak value technique has greater Fisher information than the direct technique. This is because while the fundamental limit is the same for the two methods, they are reached in different ways. Consequently, one way can be affected by the noise much more than the other. For example, we showed how the deflection measurements can strongly suppress angular jitter. We also showed that just because the direct method has higher Fisher information, does not mean that it is necessarily superior. The estimator which needs to be used to reveal the higher information may be technically difficult to implement, which would then hinder any advantage.

We then discussed two experiments using modified weak value-like techniques to precisely measure changes in frequency and phase. With only 2 mW of continuous wave input power, we have measured a frequency shift of 129 ± 7 kHz/ $\sqrt{\text{Hz}}$; we have shown that the system is stable over our maximum tuning range of 140 GHz without recalibration and is nearly shot-noise-limited. We described also our phase amplification technique. The relative phase is monitored between two paths of a slightly misaligned interferometer by measuring the average position of a split-Gaussian mode in the dark port. Although we monitor only the dark port, we show that the signal varies linearly with phase and that we can obtain similar sensitivity to balanced homodyne detection. We derive the source of the amplification both with classical wave optics and as an inverse weak value.

We then briefly reviewed some of the other topics we explored that were indirectly related to our main research goals. These included the contextual value formalism, which gives a precise prescription for how to connect the general output of a detector to the behavior of a coupled system one is interested in. We expect this approach to have great utility in a wide variety of experimental contexts. We also explored the Leggett-Garg test of quantum mechanics with weak measurements, which was a joint theory and experiment project. The contextual value approach was quite useful here, as well as in the coupled electronic Mach-Zehnder system. There, we showed how one detector's fringe information was an indirect probe for the which-path information of the other interferometer. It was also possible to implement post-selection, which may be very useful for future amplification experiments in the solid state. We also discussed some discoveries about the nature of weak values: we gave a precise interpretation to the imaginary part of the weak value, and also showed a universal form of the conditioned average away from the weak limit, so long as the von Neumann type coupling was maintained. The quantum instrument approach to systems with post-selection was also further developed.

In summary, we accomplished the main goals set out in the original proposal, and also were able to investigate a number of other related issues that arose over the course of the investigation. Although we found the weak value method does not alter the scaling of the SNR with respect to the number of photons, it still has tremendous practical advantages for many kinds of parameter estimation tasks as we have laid out.

-
- [1] Y. Aharonov, D. Z. Albert, and L. Vaidman, *Phys. Rev. Lett.* **60**, 1351 (1988); I. M. Duck, P. M. Stevenson, and E. C. G. Sudarshan, *Phys. Rev. D* **40**, 2112 (1989).
 - [2] N. W. M. Ritchie, J. G. Story, and R. G. Hulet, *Phys. Rev. Lett.* **66**, 1107 (1991).
 - [3] N. Brunner, A. Acin, D. Collins, N. Gisin, and V. Scarani, *Phys. Rev. Lett.* **91**, 180402 (2003).
 - [4] O. Hosten and P. Kwiat, *Science* **319**, 787 (2008).
 - [5] P. B. Dixon, D. J. Starling, A. N. Jordan, and J. C. Howell, *Phys. Rev. Lett.* **102**, 173601 (2009).
 - [6] M. D. Turner, C. A. Hagedorn, S. Schlamminger, and J. H. Gundlach, *Opt. Lett.* **36**, 1479 (2011).
 - [7] J. M. Hogan, J. Hammer, S.-W. Chiow, S. Dickerson, D. M. S. Johnson, T. Kovachy, A. Sugarbaker, and M. A. Kasevich, *Opt. Lett.* **36**, 1698 (2011).
 - [8] M. Pfeifer and P. Fischer, *Opt. Express* **19**, 16508 (2011).
 - [9] D. J. Starling, P. B. Dixon, A. N. Jordan, and J. C. Howell, *Phys. Rev. A* **80**, 041803 (2009).
 - [10] X. Zhou, Z. Xiao, H. Luo, and S. Wen, *Phys. Rev. A* **85**, 043809 (2012).
 - [11] D. J. Starling, P. B. Dixon, A. N. Jordan, and J. C. Howell, *Phys. Rev. A* **82**, 063822 (2010).
 - [12] D. J. Starling, P. B. Dixon, N. S. Williams, A. N. Jordan, and J. C. Howell, *Phys. Rev. A* **82**, 011802(R) (2010).
 - [13] D. J. Starling, P. B. Dixon, A. N. Jordan, and J. C. Howell, "Continuous phase amplification with a Sagnac interferometer," (2010), arXiv:0912.2357.
 - [14] G. Strübi and C. Bruder, *Phys. Rev. Lett.* **110**, 083605 (2013).
 - [15] G. I. Viza, J. Martinez-Rincon, G. A. Howland, H. Frostig, I. Shomroni, B. Dayan, J. C. Howell, arXiv:1304.0029 (2013).
 - [16] P. Egan and J. A. Stone, *Opt. Lett.* **37**, 4991 (2012).

- [17] J. Dressel, M. Malik, F. M. Miatto, A. N. Jordan, R. W. Boyd, arXiv:1305.7154 (2013).
- [18] J. C. Howell, D. J. Starling, P. B. Dixon, P. K. Vudyaletu, and A. N. Jordan, Phys. Rev. A **81**, 033813 (2010).
- [19] J. Dressel, K. Lyons, A. N. Jordan, T. M. Graham, P. G. Kwiat, Phys. Rev. A **88**, 023821 (2013).
- [20] C. M. Caves, Phys. Rev. D **23**, 1693 (1981).
- [21] S. M. Barnett, C. Fabre, and A. Maitre, Eur. Phys. J. D **22**, 513 (2003).
- [22] N. Treps, U. Andersen, B. Buchler, P. K. Lam, A. Maitre, H.-A. Bachor, and C. Fabre, Phys. Rev. Lett. **88**, 203601 (2002).
- [23] N. Treps, N. Grosse, W. P. Bowen, C. Fabre, H.-A. Bachor, and P. K. Lam, Science **301**, 940 (2003).
- [24] R. Drever, in *Quantum Optics: Experimental Gravity and Measurement Theory* (Plenum, New York, 1983) pp. 525–566.
- [25] B. J. Meers and K. A. Strain, Phys. Rev. D **43**, 3117 (1991).
- [26] D. Schnier, J. Mizuno, G. Heinzel, H. Lück, A. Rüdinger, R. Schilling, M. Schrepel, W. Winkler, and K. Danzmann, Phys. Lett. A **225**, 210 (1997).
- [27] H. Vahlbruch, S. Chelkowski, B. Hage, A. Franzen, K. Danzmann, and R. Schnabel, Phys. Rev. Lett. **95**, 211102 (2005).
- [28] A. G. Kofman, S. Ashkab, and F. Nori, Phys. Rep. **520**, 43 (2012).
- [29] M. Born and E. Wolf, *Principles of Optics* (Pergamon Press, New York, 1959).
- [30] A. N. Jordan, J. Martínez-Rincón, and J. C. Howell, arXiv:1309.5011 (2013).
- [31] R. Demkowicz-Dobrzanski, J. Kolodynski and M. Guta, Nat. Comm. **3**, 1063 (2012).
- [32] G. C. Knee, E. M. Gauger, arXiv:1306.6321 (2013).
- [33] C. Ferrie, J. Combes, arXiv:1307.4016 (2013).
- [34] A. Feizpour, X. Xingxing, and A. M. Steinberg, Phys. Rev. Lett. **107**, 133603 (2011).
- [35] Y. Kedem, Phys. Rev. A **85**, 060102 (2012).
- [36] A. Nishizawa, K. Nakamura, M.-K. Fujimoto, arXiv:1201.6039 (2012).
- [37] S. Tanaka, N. Yamamoto, arXiv:1306.2409 (2013).
- [38] H. F. Hofmann, M. E. Goggin, M. P. Almeida, M. Barbieri, Phys. Rev. A **86**, 040102(R) (2012).
- [39] L. C. Andrews and R. L. Phillips, *Laser beam propagation through Random Media*, (SPIE, Bellingham, Washington, 2005).
- [40] In this case the interaction takes the form $U = \exp(-ik\hat{A}\hat{x})$, where tracking the beam's transverse position corresponds to an imaginary weak value. We also note that while Knee and Gauger treat imaginary weak values in their Appendix B, they do not consider the addition of technical noise in this case, and further compare the Fisher information of k in the imaginary weak value case against a standard strategy measurement of x , which are different parameters.
- [41] G. C. Knee, G.A.D. Briggs, S. C. Benjamin, E. M. Gauger, Phys. Rev. A **87**, 012115 (2013).
- [42] Xiao-Ye Xu, Yaron Kedem, Kai Sun, Lev Vaidman, Chuan-Feng Li, and Guang-Can Guo, arXiv:1306.4768 (2013).
- [43] M.-L. Junttila and B. Stahlberg, Appl. Opt. **29**, 3510 (1990).
- [44] J. Ishikawa and H. Watanabe, IEEE Trans. Instrum. Meas. **42**, 423 (1993).
- [45] D. Jones, S. Diddams, J. Ranka, A. Stentz, R. Windeler, J. Hall, and S. Cundiff, Science **288**, 635 (2000).
- [46] T. Udem, R. Holzwarth, and T. W. Hansch, Nature **416**, 233 (2002).
- [47] S. Falke, H. Knöckel, J. Friebe, M. Riedmann, E. Tiemann, and C. Lisdat, Phys. Rev. A **78**, 012503 (2008).
- [48] C. Eisele, A. Y. Nevsky, and S. Schiller, Phys. Rev. Lett. **103**, 090401 (2009).
- [49] J. Dressel, S. Agarwal, and A. N. Jordan, Phys. Rev. Lett. **104**, 240401 (2010).
- [50] T. Hori, T. Matsui, K. Araki, and H. Inomata, Opt. Lett. **14**, 302 (1989).
- [51] N. Nishimiya, Y. Yamaguchi, Y. Ohnari, and M. Suzuki, Spectrochim. Acta, Part A **60**, 493 (2004).
- [52] M. Notcutt, L.-S. Ma, J. Ye, and J. L. Hall, Opt. Lett. **30**, 1815 (2005).
- [53] C. Tropea, Meas. Sci. Technol. **6**, 605 (1995).
- [54] R. Pohl *et al.*, Nature **466**, 213 (2010).
- [55] F. L. Pedrotti and L. S. Pedrotti, *Introduction to Optics*, 2nd ed. (Prentice-Hall, Inc., 1993).
- [56] I. H. Malitson, J. Opt. Soc. Am. **55**, 1205 (1965).
- [57] D. A. Steck, <http://steck.us/alkalidata/> (2010).
- [58] K.-X. Sun *et al.*, Opt. Lett. **22**, 1359 (1997).
- [59] R. Erlandsson *et al.*, J. Vac. Sci. Technol. A **6**, 266 (1988).
- [60] E. J. Post, Rev. Mod. Phys. **39**, 475 (1967).
- [61] J. Schmitt, Selected Topics in Quantum Electronics, IEEE Journal of **5**, 1205 (1999), ISSN 1077-260X.
- [62] A. Wehr and U. Lohr, ISPRS Journal of Photogrammetry and Remote Sensing **54**, 68 (1999), ISSN 0924-2716.
- [63] M. J. Holland and K. Burnett, Phys. Rev. Lett. **71**, 1355 (1993).
- [64] B. L. Higgins *et al.*, New Journal of Physics **11**, 073023 (2009).
- [65] Z. Y. Ou, Phys. Rev. A **55**, 2598 (1997).
- [66] A. Abramovici *et al.*, Science **256**, 325 (1992).
- [67] B. P. Abbott *et al.*, Reports on Progress in Physics **72**, 076901 (2009).
- [68] R. Adhikari, P. Fritschel, and S. Waldman, LIGO technical document/LIGO-T060156-01-I (2006).
- [69] J. Dressel, A. N. Jordan, Phys. Rev. A **85**, 022123 (2012).
- [70] J. Dressel, A. N. Jordan, Phys. Rev. Lett. **106**, 040402 (2011).
- [71] J. Dressel, Y. Choi, A. N. Jordan, Phys. Rev. B **85**, 045320 (2012).
- [72] E. Weisz, H. K. Choi, I. Sivan, M. Heiblum, Y. Gefen, D. Mahalu, V. Umansky, arXiv:1309.2007
- [73] J. Dressel, A. N. Jordan, Phys. Rev. A **85**, 012107 (2012).
- [74] J. Dressel, A. N. Jordan, Phys. Rev. Lett. **109**, 230402 (2012).

- [75] J. Dressel, A. N. Jordan, Phys. Rev. A **88**, 022107 (2013).